# Spin-polarized electrons in atomic layer materials formed on solid surfaces

Kazuyuki Sakamoto[a,b,*], Takahiro Kobayashi[c], Koichiro Yaji[d], Tatsuya Shishidou[e], Markus Donath[f]

[a] *Department of Applied Physics, Osaka University, Osaka 565-0871, Japan*
[b] *Center for Spintronics Research Network, Graduate School of Engineering Science, Osaka University, 560-8531, Japan*
[c] *Department of Materials and Life Science, Osaka University, Osaka 565-0871, Japan*
[d] *Research Center for Advanced Measurement and Characterization, National Institute for Materials Science, Ibaraki 305-0047, Japan*
[e] *Department of Physics, University of Wisconsin-Milwaukee, WI 53201, USA*
[f] *Physikalisches Institut, Westfälische Wilhelms-Universität Münster, 48149 Münster, Germany*

**Abstract**

In this review, we summarize the recent progress in the understanding of the spin-polarized electronic states in two-dimensional (2D) atomic layer materials (ALMs) formed on solid surfaces. The spin-polarized electronic states caused by the combination of spin-orbit coupling (SOC) with broken spatial inversion symmetry along the surface normal direction is one of the most exotic phenomena that appears on ALMs formed on solid surfaces as well as clean solid surfaces. So far, the so-called Rashba-Bychkov (RB) effect that arises from the potential gradient induced by broken inversion symmetry was believed to be the main origin of these spin-polarized electronic states. However, the spin texture of most ALMs are different from that caused by the ideal RB effect. Due to the high impact of the spin-polarized electronic states of 2D materials in not only spin-related fundamental science but also in applications since they are the key concepts to realize future semiconductor spintronics devices, much efforts have been made to elucidate the origin of these peculiar spin textures. So far, the deviations in spin texture from the ideal one have been attributed to be induced

*Corresponding author
*Email address:* kazuyuki_sakamoto@ap.eng.osaka-u.ac.jp (Kazuyuki Sakamoto)

by perturbation, such as entanglement of spin and orbital momenta. In this review, we first illustrate how the symmetry of the ALM's atomic structure can affect the spin texture, and then introduce that various spin textures, ranging from the RB-type and symmetry-induced type to spin textures that cannot be explained based on the origins proposed so far, can be simply induced by the orbital angular momentum. This review aims to provide an overview on the insights gained on the spin-polarized electronic states of ALMs and to point out opportunities for exploring exotic physical properties when combining spin and other physics, e.g. superconductivity, and to realize future spintronics-based quantum devices.

*Keywords:* Atomic layer materials, Rashba effect, spin-polarized band, symmetry, orbital angular momuntum

## 1. Introduction

Two-dimensional (2D) atomic layer materials (ALMs) formed on solid surfaces show exotic quantum phenomena that do not appear in 3D bulk systems, and thus have attracted an incredible interest in the past decade. The formation of ALMs on solid surfaces also allows to create 2D materials that do not exist in nature. The graphene family silicene [1], germanene [2, 3], borophene [4, 5], which can not survive as free standing ALM but can be formed on Ag(111) or Al(111) surfaces, have been reported to host massless Dirac Fermions, and the atomic layer FeSe formed on $SrTiO_3$ shows a 10 times higher superconducting transition temperature than that of bulk FeSe [6]. The combination of broken spatial inversion symmetry along the surface normal direction (i.e. one side of the ALM is the substrate and the other side is vacuum or air or liquid as shown in Fig. 1(a)) and spin-orbit coupling (SOC) leads to further exotic phenomena for these ALMs, which related to electron spins that are of interest for not only fundamental science but also applications since they contain key concepts needed to realize future semiconductor spintronics devices [7, 8, 9, 10, 11, 12, 13].

In case of a nonmagnetic "ideal" 2D electron gas, the bands of electron with

opposite spin direction are degenerate and show a parabolic dispersion following the equation,

$$E_B(\vec{k}_{||}) = \frac{\hbar^2}{2m^*}\vec{k}_{||}^2 \tag{1}$$

as shown in Fig. 1(b), where $\vec{k}_{||} = (k_x, k_y, 0)$ ($k_{||} = \sqrt{k_x^2 + k_y^2}$) and $m^*$ are the momentum parallel to the 2D plane and the effective mass, respectively. The spin degeneracy in this 2D gas results from the presence of both the time-reversal and the spatial inversion symmetries, which can be expressed as $E_B(\vec{k}_{||}, \uparrow) = E_B(-\vec{k}_{||}, \downarrow)$ and $E_B(\vec{k}_{||}, \uparrow) = E_B(-\vec{k}_{||}, \uparrow)$ ($\uparrow$ and $\downarrow$ indicate up-spin and down-spin). That is, the only solution to satisfy the two symmetries simultaneously is $E_B(\vec{k}_{||}, \uparrow\downarrow)) = E_B(-\vec{k}_{||}, \uparrow\downarrow)$, which means that the band of the up-spin has the same dispersion as that of the down-spin. However, in case of having one of the two symmetries broken, this spin degeneracy is lifted. When the spatial inversion symmetry is broken, i.e. $E_B(\vec{k}_{||}, \uparrow) \neq E_B(-\vec{k}_{||}, \uparrow)$, the effect of SOC can basically be explained by the so-called Rashba-Bychkov (RB or simply Rashba) effect [14]. The RB Hamiltonian can be expressed as

$$H_{RB} = \alpha_R(|\varepsilon|)\ \vec{\sigma} \cdot (\vec{k}_{||} \times \hat{e}_z), \tag{2}$$

where, $\hat{e}_z = (0, 0, 1)$, $\alpha_R$ is the Rashba parameter ($\alpha_R = \hbar^2 k_0/m^*$; $k_0$ is the offset by which the $E(\vec{k}_{||})$ parabola is shifted away from the time-reversal invariant momenta such as the $\bar{\Gamma}$ point of the Brillouin zone), and $\varepsilon$ is an electric field determined by the potential gradient normal to the surface. This RB effect splits the band of a nonmagnetic electron 2D gas into two parabolas along the momentum direction, whose dispersion follows the equation

$$E_B(\vec{k}_{||}) = \frac{\hbar^2}{2m^*}\vec{k}_{||}^2 \pm \alpha_R\vec{k}_{||}, \tag{3}$$

as shown in Fig. 1(c). Furthermore, as can be understood by the RB Hamiltonian, the split band is spin-polarized with the spin polarization vector ($\vec{P}$) parallel to the 2D plane and perpendicular to the momentum, and the directions of $\vec{P}$ of the two bands are opposite, i.e. $\vec{P}(\vec{k}_{||}) = -\vec{P}(-\vec{k}_{||})$ (Fig. 1(c)). This ideal RB-type spin splitting was observed in the L gap of the (111) surface

of Au, Ag, and Cu [15, 16, 17, 18, 19, 20, 21, 22], but with energy splitting much larger than that expected for a 2D electron gas. Taking into account the average potential gradient $\sim 1$ eV/Å on metal surfaces, the Rashba parameter $\alpha_R$ is in the order of $\sim 10^{-6}$ eVÅ for a 2D electron gas. This means that the splitting would be only a few $\mu$eV even at the boundary of the Brillouin zone, where the splitting would be largest, while the splitting observed at the Fermi wave vectors are 110 meV on Au(111) [15], 5 meV on Ag (111) [22] and 16 meV on Cu(111) [22]. Further large Rashba-type spin splittings were observed on ALMs formed on solid surfaces [23, 24, 25, 26], and it has been argued that they are originating from a local asymmetric charge distribution along the direction normal to the 2D layer in close proximity to the nuclei of the surface atoms [23, 27], where the essential role of inversion symmetry breaking is to mix different parity states. In contrast to these reports, in which the spin-textures are similar to that of an ideal RB effect, spin textures that differ from the ideal case have been reported for several ALMs in e.g. Refs. [28, 29, 30, 31, 32, 33, 34, 35, 36, 37, 38, 39, 40]. The origins of these peculiar spin textures were attributed to, e.g. the perturbation induced by the entanglement of spin and orbital momenta, but they are still explained within the framework of the RB effect [26, 38, 41, 42].

This review aims to provide an overview on the insights gained on the spin-polarized electronic states of ALMs and to point out opportunities for exploring exotic physical properties when combining spin and other physics, e.g. superconductivity, and to realize future spintronics-based quantum devices. Here, we present two novel effects that go beyond the framework of the RB effect for creating spin-polarized bands in ALMs formed on solid surfaces. The first effect is the geometric symmetry of the atomic structure [28, 29, 32, 33, 35, 43] and the second one is the orbital angular momentum (OAM) of valence electrons [40]. The geometric symmetry was not considered to affect the"RB spins" in the early studies (for example Refs. [24, 15, 16, 20, 44, 45, 46, 47, 48, 49, 50]), but it is now considered to have influence on the spin texture, and is expected to be a necessary condition to gain a proper understanding on the spin texture in recent studies (for example Refs. [30, 39, 51, 52, 53, 54, 55, 56, 57, 58, 59, 60]).

Below, we focus on the effects of three different symmetries $C_3$, $C_{3v}$ and $C_{1h}$ (the relation between the symmetry of the crystal and that of the $k$ point is shown in Table 1), and show the peculiar spin textures originated from them. Regarding the OAM, the so-called chiral OAM has been reported to play a role in defining the size of the spin splitting [26, 41, 42], but not so much to the spin texture. (Here we use "chiral OAM" as an effect that produces spin texture similar to that of the RB effect.) In this review we will show that various spin textures, ranging from the RB-type and symmetry-induced type, can be induced by the OAM. A fundamental understanding of the spin physics arising from the SOC in ALMs is necessary for the realization of not only semiconductor spintronics and/or quantum devices [7, 10, 12], but also for possible novel physical properties such as topological superconductors formed by 2D materials with spin-polarized states [61, 62, 63].

Table 1: Relation between the 2D lattice (plane group) and the symmetry at the $k$ points with high symmetry.

| lattice (plane group) | $k$ points | symmetry |
|---|---|---|
| triangular ($p3m1$) | $\bar{\Gamma}$ | $C_{3v}$ |
| | $\bar{K}$ | $C_3$ |
| | $\bar{M}$ | $C_{1h}$ |
| triangular ($p31m$) | $\bar{\Gamma}, \bar{K}$ | $C_{3v}$ |
| | $\bar{M}$ | $C_{1h}$ |
| rectangular ($p1m1$) | $\bar{\Gamma}, \bar{X}, \bar{X}'$ | $C_{1h}$ |

## 2. Overview of the experimental setup and theoretical calculation

### *2.1. Spin and angle-resolved photoelectron spectroscopy*

Angle-resolved photoelectron spectroscopy (ARPES) is the most appropriate technique to determine the occupied band structure of materials, and spin-resolved ARPES (SARPES) gives further information about its spin degree of freedom. A typical setup for ARPES and SARPES measurements is shown in

Fig. 2. Photoelectrons excited by different light sources (a vacuum-ultraviolet (VUV) laser ($h\nu$ =6.994 eV), a He discharge lamp ($h\nu$ =21.22 or 40.81 eV), or synchrotron radiation light (beamline I4 at MAX-lab, Sweden and the APE beamline at Elettra, Italy: $h\nu = 15 - 40$ eV)) were collected by hemispherical photoelectron analyzers. For ARPES measurements, the photoelectrons that passed through the hemispherical analyzer go directly to a 2D detector. The 2D detector makes possible to obtain the relation between the kinetic energy of photoelectrons ($E_k$) and their emission angle ($\theta_e$), which corresponds to the binding energy ($E_B$) of electron along a certain $\vec{k}_{||}$ direction, i.e. the band dispersion. The relation between $E_B$ and $E_k$ can be expressed as $E_B = h\nu - E_k - \phi$ and $\vec{k}_{||} = (\sin\theta_e/\hbar)\sqrt{2mE_k}$, where $\phi$ is the work function of the sample, $m$ is the electron mass and $E_k$ is the kinetic energy of the photoelectron. In case of SARPES measurements, photoelectrons are guided to the spin detector by using a deflector lens after passing through the hemispherical analyzer, and detected using electron counters. All occupied states band structures shown in this review have been obtained by high-resolution ARPES and SARPES measurements performed in different ultrahigh vacuum (UHV) chambers under base pressure of $< 1 \times 10^{-8}$ Pa. The energy and momentum resolutions were 3 meV and $1.4 \times 10^{-3}$ Å$^{-1}$ for the measurements using VUV laser, $10 - 25$meV and $< 5 \times 10^{-3}$ Å$^{-1}$ when using other light sources for ARPES, and 20 meV and $2.1 \times 10^{-2}$ Å$^{-1}$ (VUV laser) and $20 - 200$ meV and $2.2 \times 10^{-2} - 6 \times 10^{-2}$ (other light source) for SARPES. The sample was maintained at between 35 and 100 K during all ARPES measurements.

### *2.2. Spin- and angle-resolved inverse photoemission*

The unoccupied spin-polarized electronic bands have been measured by spin- and angle-resolved inverse photoemission (SARIPE) at the Westfälische Wilhelms-Universität Münster, Germany [64, 65]. In a multi-chamber ultra-high vacuum apparatus with base pressure below $3 \times 10^{-9}$ Pa, spin-polarized electrons of energies between 7 and 15 eV were emitted from a GaAs photocathode and directed with defined $k$ vector onto the sample. The electrons can undergo

radiative transitions into lower-lying unoccupied states at the sample surface, thereby emitting photons. In our experimental setup, photons with an energy of 9.9 eV are detected via bandpass detectors, while varying the kinetic energy of the incoming electrons. The energy resolution was approximately 350 meV [66, 67], and the momentum resolution was 0.06 $\text{Å}^{-1}$ for states close to the Fermi level [68, 69]. This Bremsstrahlung process in the VUV region is the time-reversed process of the photoelectric effect used for ARPES. Adding spin detection/preparation and combining both methods, SARPES and SARIPE, enabled us to determine the spin-dependent electronic bands below and above the Fermi level, in particular within the interesting energy region around the Fermi level.

### *2.3. Sample preparations*

A Si(111) sample (Sb-doped $n$-type, $\rho = 1-5\ \Omega\cdot\text{cm}$) was used as a substrate to create Tl ALM and Bi ALM, a Si(110) sample (B-doped $p$-type, $\rho = 1-5$ $\Omega$cm) for another Tl ALM and a Si(111) sample ($n$-type, $\rho = 1-5\ \Omega\cdot\text{cm}$) with a 1.5° miscut towards the $[\bar{1}\bar{1}2]$ direction was used for the In ALM. The on-axis Si(111) (the one without a miscut) and the Si(110) samples were cleaned by first degassed at 900 K for more than 5 h and then annealed up to 1520 K for a few seconds in a vacuum chamber using direct resistive heating, and the vicinal Si(111) surface was cleaned following the procedure described in Refs. [70] and [71]. After the annealing, a sharp (7×7) or (16×2) low-energy electron diffraction (LEED) pattern was observed, and neither the valence-band spectra nor the core-level spectra showed any indication of contamination.

The Tl (Bi) ALM was formed by depositing one monolayer (ML) of Tl (Bi) on a clean Si(111)-(7×7) surface from a Knudsen cell at a substrate temperature of 570 K and the other Tl ALM was obtained by depositing 1 ML of Tl on a Si(110)-(16×2) clean surface at a substrate temperature of 450 K. The In ALM was prepared by depositing approximately 3 monolayers of In onto a clean Si(111) surface at 300 K, followed by annealing at 600 K for a couple minutes. The atomic periodicity in Tl ALMs on Si(111) and Si(110) are the

same one as those in bulk, i.e. their structure can be described as Tl/Si(111)-(1×1) and Tl/Si(110)-(1×1), and the superstructure formed by the Bi and In ALMs show Bi/Si(111)-($\sqrt{3} \times \sqrt{3}$) and In/Si(111)-($\sqrt{7} \times \sqrt{3}$) structures. The sample quality of all ALMs was confirmed by the observations of sharp spots with low background intensity in LEED and sharp electronic states in ARPES spectra.

### *2.4. Density functional theory (DFT) calculation*

The theoretical calculations for all ALMs are based on the first-principles density-functional approach. Calculations were carried out by using the generalized gradient approximation [72] in the Kohn-Sham theory [73], which employs ultra-soft pseudo-potentials [74] and plane waves, for Tl/Si(111) and Tl/Si(110), and based on the first-principles density-functional approach, in which one electron Kohn-Sham equations are solved with the all-electron full-potential linear augmented-plane-wave (FLAPW) method including the SOC as a second variation in self-consistent-field iterations for Bi/Si(111). Energy cutoffs of 25 and 300 Ry for wave functions and densities [75], and a repeated slab model, in which each slab contains a Tl ML, a H ML and 24 Si ML for Tl/Si(111) and Bi/Si(111). A smaller number of Si layer, 16 Si ML, was used for Tl/Si(110). Regarding the In/Si(111), the FLAPW method [76] as implemented in the HiLAPW code was used with the local density approximation, where the wave function and potential cutoffs were 14 and 100 Ry, respectively, and the repeated slab model contains 2 In ML, a H ML and 8 Si ML.

## 3. Results and Discussion

### *3.1. Symmetry induced spin-polarized bands*

#### *3.1.1. $C_3$ symmetry*

In this sub-subsection, we discuss the effect of the $C_3$ symmetry by considering the spin-polarized bands of Tl/Si(111)-(1×1). As shown in the schematic illustration of the atomic structure of Tl/Si(111)-(1×1) (Figs. 3(a) and (b)),

Tl atoms are adsorbed on the $T_4$ site of a Si(111)-(1×1) ideal surface, i.e. the threefold hollow site of the first layer Si atoms, ontop of the second layer Si atoms [77, 78]. This adsorption site leads the structure of Tl/Si(111)-(1×1) to belong to the $p3m1$ plane group, where the primitive lattice vector of the $1 \times 1$ unit cell is rotated 30° from the mirror plane, and thus the $\bar{\Gamma}$, $\bar{M}$ and $\bar{K}$ points of the Brillouin zone to have $C_{3v}$, $C_{1h}$ and $C_3$ symmetries, respectively. The $\bar{\Gamma}$, $\bar{M}$ and $\bar{K}$ points are shown in Fig. 3(c) together with the LEED pattern of Tl/Si(111)-(1×1).

Figure 4(a) shows the band structure of Tl/Si(111)-(1×1) along the $\bar{\Gamma} - \bar{K}$ direction obtained experimentally by ARPES, SARPES and SARIPE together with the band structure obtained theoretically. The band, which is spin-degenerate and located at $E_B \sim 0.25$ eV at the $\bar{\Gamma}$ point, evolves into a pair of spin-split bands away from $\bar{\Gamma}$. The spin texture of these bands has been revealed by SARPES measurements. As shown in Figs. 4(b) and (c), the two spin-polarized bands for $\vec{P}$ parallel to the surface and perpendicular to $\vec{k}_{||}$ and those for $\vec{P}$ perpendicular to the surface overlap at $\theta_e = 0°$, indicating that the two spin-polarized bands are degenerate at the $\bar{\Gamma}$ point. At $\theta_e = 10°$, which corresponds to $\vec{k}_{||} \sim 0.36$ Å$^{-1}$, the peak positions of the two spin-polarized spectra are different in Fig. 4(b) while they are the same in (c). The splitting in peak position of SARPES spectra with $\vec{P}$ parallel to the surface and perpendicular to $\vec{k}_{||}$, and the overlap of the two SARPES spectra with $\vec{P}$ perpendicular to the surface were obtained till $\theta_e = 26°$ that corresponds to $\vec{k}_{||} \sim$0.87 Å$^{-1}$. This means that the $\vec{P}$ of the two spin-split bands is parallel to the surface and perpendicular to $\vec{k}_{||}$ till $\vec{k}_{||} \sim$0.87 Å$^{-1}$, and therefore behaves like an ordinary RB type spin-polarized band structure in this $\vec{k}_{||}$ region. (Note that although the experimentally detected spin information is not necessarily the spin polarization of the initial (final) state but may be influenced by the transition matrix element which includes the final (initial) state as well as experimental parameters such as the geometry (light polarization and incidence (detection)angle [25, 59, 79, 80] all spin information shown in this review are confirmed by theoretical calculation.)

In contrast to the $\vec{P}$ from $\vec{k}_{||} = 0$ to ∼0.87 Å$^{-1}$, the $\vec{P}$ at larger $\vec{k}_{||}$ shows

a completely different behavior. As shown in the spectra measured at $\theta_e = 34°$, which corresponds to a $\vec{k}_{||}$ close to the $\bar{K}$ point, the two spin-polarized spectra with ideal RB type $\vec{P}$ are overlapped, whereas the peaks of the two spectra with $\vec{P}$ perpendicular to the surface are split. These results indicate that the $\vec{P}$ of the band, which lies in the surface, rotates and points along the direction perpendicular to the surface around the $\bar{K}$ point. Furthermore, the spin polarization obtained around the $\bar{K}$ point is 100 %, a value larger than that expected from an ideal or simple RB effect. The 100 % spin polarization is obtained after subtracting the background intensity, and was confirmed by theoretical calculation. The spin-split bands with $\vec{P}$ pointing along the surface normal direction are also observed above the Fermi level, indicating that this is a peculiar effect at the $\bar{K}$ point. Figure 4(d) displays the corresponding SARIPE spectra with 100 % out-of-plane spin-polarized Tl-induced bands and a splitting of ∼0.6 eV at the $\bar{K}$ point.

The 100 % spin-polarized band with $\vec{P}$ pointing along the surface normal direction cannot be explained by the simple RB effect described in eq. (2). In order to understand the origins of this peculiar $\vec{P}$, we expand the RB effect in a real 2D system such as ALM formed on solid surfaces, i.e. we consider the periodic atomic structure of the 2D system instead of a simple 2D electron gas. Using Bloch wave functions $\varphi_{n\vec{k}}(\vec{r}) = (1/\sqrt{\Omega})\exp(i\vec{k}\cdot\vec{r})u_{n\vec{k}}(\vec{r})$, and by considering that the Coulomb interaction from the nucleus is the main factor acting to the potential on electrons, i.e. $\nabla V(\vec{r}) \approx \frac{1}{r}\frac{dV(\vec{r})}{dr}\vec{r}$, the effective SOC Hamiltonian can be described as

$$\begin{aligned} \mathscr{H}_{SOC}(\vec{k}) &= \langle\varphi_{n\vec{k}}(\vec{r})|\,\frac{\hbar}{4m_e^2c^2}\vec{\sigma}\cdot(\nabla V(\vec{r})\times\vec{p})\,|\varphi_{n\vec{k}}(\vec{r})\rangle \\ &= \vec{\sigma}\cdot(\vec{\alpha}_n(\vec{k})\times\vec{k}) + \vec{\sigma}\cdot\vec{B}_n(\vec{k}) \end{aligned} \tag{4}$$

where

$$\vec{\alpha}_n = \frac{\hbar^2 N}{4m_e^2c^2\Omega}\int_{cell} d\vec{r}|u_{n\vec{k}}(\vec{r})|^2\nabla V(\vec{r}) \tag{5}$$

$$\vec{B}_n(\vec{k}) \approx \frac{\hbar^2 N}{4m_e^2c^2\Omega}\int_{cell} d\vec{r}\left(\frac{1}{r}\right)\left(\frac{dV(\vec{r})}{dr}\right)u^*_{n\vec{k}}(\vec{r})(\vec{\ell})u_{n\vec{k}}(\vec{r}). \tag{6}$$

The first term of eq. (4) is the RB term, and the second term, which is not considered in the case of an ideal 2D system, is a Zeeman term that acts as an effective magnetic field to the band spin magnetization. As one notice from eq. (6), the field $\vec{B}_n(\vec{k})$ is obtained as an averaged value on the angular momentum operator ($\vec{\ell}$), and is mainly caused by the atomic character of the wave function. This field $\vec{B}_n(\vec{k})$ can have a large finite value, when the wave function $u_{n\vec{k}}(\vec{r})$ is a good quantum state of the angular momentum operator, and as a result, the electron spin tends to become parallel to the direction of $\vec{B}_n(\vec{k})$.

The hypothetical direction of $\vec{P}$ of one of the spin split bands, as derived from the normal RB effect (eq. (2) and the first term of eq. (4)), is illustrated in Fig. 4(e). As shown in this figure, when the $\vec{P}$ of one of the band rotates anticlockwise around $\bar{\Gamma}$, the spin texture of this band can be clockwise around $\bar{M}$. In this simple picture, $\vec{P}$ points along the same direction from $\bar{\Gamma}$ to $\bar{K}$ as from $\bar{K}$ to $\bar{M}$ of the next Brillouin zone (note that $\bar{K}$ is a $\vec{k}_{||}$ point without time-reversal symmetry and $\vec{P}$ changes its sign to $-\vec{P}$ in case of crossing a $\vec{k}_{||}$ point with time-reversal symmetry as shown in Fig. 1(c)). This means that $\vec{P}$ of the normal RB spin is indeterminable at the $\bar{K}$ point, and indeed, the first term of eq. (4) is found to vanish at $\bar{K}$ owing to its $C_3$ symmetry in the theoretical study and only the second term contributes to the spin polarization at the $\bar{K}$ point. Taking into account that the function $p_x - ip_y$ (or $p_x + ip_y$) forms an irreducible representation of the $C_3$ group when SOC is neglected, i.e. electrons make a circular motion in the $xy$ plane at a $\vec{k}_{||}$ point with $C_3$ symmetry, the effective field of $\vec{B}_n(\vec{k})$ becomes parallel to the $z$ direction at $\bar{K}$. Thus, when the SOC is on, the interaction lifts the spin degeneracy and leads $\vec{P}$ to be perpendicular to the surface. As an example of this structure-induced twisting of the spin, we followed the spin polarization of the unoccupied surface state around the $\bar{M}$ point. While crossing the $\bar{\Gamma}\bar{M}$ line, the spin is exclusively of RB type, i.e., within the surface plane and perpendicular to $k_{||}$. While crossing the $\bar{K}\bar{M}$ line, the spin rotates to out of plane. In a"walk" around the $\bar{M}$ point, the spin is found to be twisted in a peculiar way [55]. This result indicates that, the symmetry of the surface plays a significant role in the spin-polarized states of 2D systems.

($k$ points with $C_2$ and $C_4$ symmetries were also theoretically predicted to show spin with $\vec{P}$ perpendicular to the surface [43], but this unique behavior was only experimentally confirmed at $k$ points with $C_3$ symmetry [28, 32, 33, 54, 57].)

Although a 100 % spin-polarized band is of great importance for the realization of semiconductor spintronics devices, the occupied bands at the $\bar{K}$ point are far below the Fermi level and will, therefore, hardly contribute to any charge transport. On the other hand, the spin-polarized unoccupied bands at $\bar{K}$ are located just above the Fermi level with a substantially large spin splitting of 0.6 eV. This suggests a possibility to easily make a metallic spin-polarized valley band, which can produce spin-charge transport, by doping electrons into the Tl/Si(111)-(1×1) surface while keeping the substrate semiconducting. Figure 5(a) shows the band structure at the $\bar{K}$ point of Tl/Si(111)-(1×1) with an additional Tl coverage of 0.12 ML. The spin polarization at this valley has been confirmed to be 100 % and the $\vec{P}$ to be perpendicular to the surface by SARPES, i.e. the spin features do not change upon doping, as shown in Fig. 5(b). Furthermore, the spin-polarization vectors at $\bar{K}$ and $\bar{K}'$ have been obtained to be opposite (this can be understood by the presence of time-reversal symmetry; $E_B(\vec{k}_{||}, +\vec{P}) = E_B(-\vec{k}_{||}, -\vec{P})$), i.e. spins of the valley point outward the surface at $\bar{K}$, and those point inward the surface at $\bar{K}'$. As shown in Fig. 5(c), these 100 % spin-polarized valleys with opposite $\vec{P}$ at $\bar{K}$ and $\bar{K}'$ can act as filters that suppress the backscattering of spin-charge. The creation of spin-polarized valley using the symmetry of the atomic structure is much easier and simpler than those proposed previously for valley polarization in graphene [81, 82] that require almost unrealistic procedures.

*3.1.2. $C_{3v}$ symmetry*

Here, we discuss the spin-polarized bands of $\beta$-Bi/Si(111)-($\sqrt{3} \times \sqrt{3}$). Figures 6(a) and (b) show the top view and side view of $\beta$-Bi/Si(111)-($\sqrt{3} \times \sqrt{3}$) [83, 84, 85]. (This atomic structure is known as the so-called milk stool model [86].) The center of gravity of the three Bi atoms forming a trimer is on the $T_4$ site of a Si(111)-(1×1) ideal surface. As shown in Fig. 6(a), the primitive

lattice vector of the $\sqrt{3} \times \sqrt{3}$ unit cell is parallel to the mirror plane, which indicates the structure of this system to belong to the $p31m$ plane group, a group that is different from that of the Tl/Si(111)-(1×1) surface. Since the $\bar{K}$ point of the Brillouin zone is located on the mirror plane (6(c)), both the $\bar{\Gamma}$ and $\bar{K}$ points have a $C_{3v}$ symmetry, and the $\bar{M}$ point has a $C_{1h}$ symmetry on $\beta$-Bi/Si(111)-($\sqrt{3} \times \sqrt{3}$).

The band structure of $\beta$-Bi/Si(111)-($\sqrt{3} \times \sqrt{3}$) along $\bar{\Gamma} - \bar{M} - \bar{\Gamma} - \bar{K} - \bar{M}$ is shown in Fig. 7. Three states are clearly observed at $E_B$ of 1.25 eV, 1.45 eV, and 1.83 eV at the $\bar{\Gamma}$ point of the second Brillouin zone ($\vec{k}_{||} = -1.09$ Å$^{-1}$) and at 0.53 eV, 0.91 eV, and 1.35 eV at the $\bar{M}$ point along the $\bar{\Gamma}$-$\bar{M}$-$\bar{\Gamma}$ direction. All these three states, whose number agrees well with those reported in former studies [50, 87, 88], follow a ($\sqrt{3} \times \sqrt{3}$) periodicity. (Note that although the number of observed states is the same, the dispersions reported in Refs. [87] and [88] are different from the present ones probably due to the lower energy and angular resolutions of the system and/or the lower sample quality used in those study.) Among these three states, the two with lower $E_B$ show clear RB-type splittings at the $\bar{M}$ point and the RB-type splitting of the one with highest $E_B$ is clearly observed at the $\bar{\Gamma}$ point of the second Brillouin zone. The filled circles overlapping the experimental data are the calculated bands, and their size represents the degree of $\vec{P}$ whose direction corresponds to that of an ideal RB spin (red and yellow indicate spins with opposite $\vec{P}$). (Some small filled circles are not observed experimentally due to their small cross section, which result from the energy and/or polarization of the light used in the present study, or from the large bulk contribution of these states.) The calculated split bands show clear opposite spin polarization for the three bands around the $\bar{M}$ and $\bar{\Gamma}$ points. Taking into account that the direction of $\vec{P}$ is parallel to the surface and perpendicular to $\vec{k}_{||}$, the splittings observed along the $\bar{\Gamma}$-$\bar{M}$-$\bar{\Gamma}$ direction look to originate from the normal RB effect. In this case, the Rashba parameters, $\alpha_R$, are ∼2.3 eVÅ and ∼1.7 eVÅ for the lowest and second lowest $E_B$ states at the $\bar{M}$ point and ∼1.5 eVÅ for the highest $E_B$ state at the $\bar{\Gamma}$ point. (The $\alpha_{\mathrm{R}}$ of the lowest $E_B$ state shows good agreement with the value reported in Ref. [50].)

The spin splittings are also observed along the $\bar{\Gamma} - \bar{K} - \bar{M}$ direction.

$\bar{K}$ is a point without time-reversal symmetry, i.e. $\vec{q} \neq \vec{G}/2$ and thus $E(\vec{q}+\vec{k},\vec{P}) \neq E(\vec{q}-\vec{k},-\vec{P})$ at $\bar{K}$. This means that there should be no RB splitting around the $\bar{K}$ point of the Brillouin zone, because the time-reversal symmetry ($E(\vec{q}+\vec{k},\vec{P}) = E(\vec{q}-\vec{k},-\vec{P})$) was regarded as a necessary condition for RB splitting. Regarding the split band at lowest $E_B$, however, the band marked by yellow is above the band marked by red in the $k_{//}$ range from $\bar{\Gamma}$ to $\bar{K}$, and the yellow band is below its counterpart from $\bar{K}$ to $\bar{M}$. This means that there is a RB-type spin splitting around $\bar{K}$ though this point does not have time-reversal symmetry. In order to understand the origin of the spin splitting around $\bar{K}$, we discuss the symmetry at this point on the basis of group theory. As mentioned above, the symmetry at $\bar{K}$ is $C_{3v}$, i.e. the same symmetry as that at $\bar{\Gamma}$ on $\beta$-Bi/Si(111)-($\sqrt{3} \times \sqrt{3}$). The 2D irreducible representation of the $C_{3v}$ group reveals the isotropic spin splitting and vortical spin structure that is given by the RB Hamiltonian regardless of the existence of time-reversal symmetry [43]. This means that the split observed around $\bar{K}$ would be a RB-type spin splitting, but which is referred as a peculiar RB splitting in the sense that it is not accounted for the time-reversal symmetry that was believed to be a necessary condition for RB splitting, but by the consequence of the point group symmetry.

In Fig. 8, we show the constant energy contours of the lowest $E_B$ state around the $\bar{M}$ and $\bar{K}$ points. The $E_B$ of the constant energy contours are 0.85 eV in (a) and 0.45 eV in (b). The dashed lines are the boundaries of the Brillouin zone and the filled circles show the symmetry points of the Brillouin zone. In contrast to a constant energy contours formed by a normal RB effect, those observed in Fig. 8(a) are quite distorted and those in (b) are not closed. However, despite of their distorted shape, the closed structure in Fig. 8(a) indicates that the lowest $E_B$ state shows a vortical type spin structure around the $\bar{K}$ point that has been confirmed by theoretical calculation. (The distorted shapes would originate from the crystal field that is generally stronger at the boundary of the Brillouin zone.) Taking the vortical spin structure around $\bar{K}$ and the $C_{3v}$ symmetry of this point into account, we conclude the spin splitting observed around the

$\bar{K}$ point to definitely result from a peculiar RB effect that is given without a time-reversal symmetry, which was believed to be a necessary condition for RB splitting.

The presence of vortical spin structures around both the $\bar{K}$ and $\bar{\Gamma}$ points lead to a non-vortical spin structure at the $\bar{M}$ point as shown in the schematic illustration of Fig. 8(c). The arrows in Fig. 8(c) show the $\vec{P}$ of one of the split bands, as derived from the normal RB effect. This non-vortical spin structure, which is observed as hyperbolic curves in the constant energy contour shown in Fig. 8(b), indicates the presence of a peculiar RB splitting at the $\bar{M}$ point, a point with time-reversal symmetry, and therefore demonstrates that the time-reversal symmetry is not a sufficient condition to obtain a normal RB splitting with vortical spin structure. These results on $\beta$-Bi/Si(111)-($\sqrt{3} \times \sqrt{3}$) imply that the time-reversal symmetry is not a necessary and sufficient condition for a spin-splitting and once again that knowledge on the 2D symmetry of the system is indispensable to understand the RB effect properly.

### *3.1.3. $C_{1h}$ symmetry*

As discussed in the previous subsection, a $k$ point with $C_{1h}$ symmetry holds the potential to yield a novel spin structure [43]. In particular, the occurrence of $C_{1h}$ symmetry at the $\bar{\Gamma}$ point is expected to give rise to a peculiar spin structure that is insensitive to backscattering and therefore along with long spin coherence [32, 89]. To obtain a system whose $\bar{\Gamma}$ point has $C_{1h}$ symmetry and shows a RB splitting, both a substrate with a proper symmetry and an appropriate adsorbate are indispensable. Here, we used the Si(110) surface as a substrate, whose ideal (1×1) structure has a mirror plane, a glide plane and a rotation center and thus belong to the *p2mg* plane group. (The clean Si(110) surface has a (16×2) periodicity and a complex structure, e.g. [90, 91, 92, 93, 94].) The adsorption of 1 ML of Tl kills the glide plane and the rotation center, and leads the formation of a (1×1) structure that belongs to the *p1m1* plane group, which corresponds to a system whose $\bar{\Gamma}$ point has a $C_{1h}$ symmetry in $\vec{k}$ space. The loss of glide symmetry is in agreement with the observation of all fundamental

LEED spots along the [1$\bar{1}$0] direction (Fig. 9(c)). (Every second fundamental spot disappears in case of having a glide symmetry.) The break of the *p2mg* symmetry of the ideal surface into a *p1m1* one results from the presence of two adsorption sites of Tl atoms with different height from the outermost Si atom as shown in Figs. 9(a) and (b). This atomic structure was obtained experimentally by a LEED I-V measurement and was confirmed by the optimized structural model obtained by DFT calculation [35].

Figures 10(a) displays the band dispersion of Tl/Si(110)-(1×1) along the $\bar{X}'$-$\bar{\Gamma}$-$\bar{X}'$ direction. A clear RB-type splitting is observed in the uppermost band that shows an upward dispersion from $\bar{\Gamma}$ to $\vec{k}_x \sim \pm 0.3$ Å$^{-1}$ and then a downward dispersion till $\bar{X}'$. The maximum $E_B$ separation of these RB-type split band is $\Delta E_B = 150$ meV at $k_x = -0.28$ Å$^{-1}$. The constant energy contours of this uppermost band at $E_B$ =50, 100 and 200 meV are shown in Figs. 10(b), (c) and (d), respectively. The characteristic constant energy contours of this state are the dumbbell shape at $E_B = 50$ meV, the peanut shape at $E_B$ =100 meV and the butterfly shape at $E_B = 200$ meV. These shapes are totally different from the constant energy contours of an ordinary RB effect that show two concentric circles with their center at a $\vec{k}_{||}$ point with time-reversal symmetry as shown in Fig. 1(c). The absence of closed constant energy contour around $\bar{\Gamma}$ arises from the anisotropic band structure that originates from the lack of rotational symmetry, and therefore from the $C_{1h}$ symmetry at $\bar{\Gamma}$ of this system.

The $\vec{P}$ of the RB bands obtained by DFT calculation is superimposed on the constant energy contour at $E_B$ =100 meV in Fig. 11(a). As shown in this figure, two ellipses of opposite $\vec{P}$ that are symmetric with respect to the $\bar{\Gamma}$ point are found in this system. $\vec{P}$ points toward the $-y$ ($+y$) direction at $k_x < 0$ ($k_x > 0$) within an angle deviation of less than 16° to the $x$ ($-x$) direction, and less than 5° to the surface normal direction $z$ ($-z$). This result means that each elliptical constant energy contour has $\vec{P}$ along nearly the $y$ direction. Although the sign reversal of $\vec{P}$ at $\pm k_x$ indicates the RB splitting to be like an ordinary one along the $\bar{\Gamma}$-$\bar{X}'$ direction, by considering the time-reversal symmetry of the $\bar{\Gamma}$ point, the results in Fig. 11(a) show that the spin structure is non-vortical unlike

the ordinary RB effect. This non-vortical spin structure has been confirmed experimentally as well. The SARPES spectra measured at $k_x = 0.16$ and $-0.27$ Å$^{-1}$ at $k_y = 0$ and at $k_y = 0.25$ and $-0.37$ Å$^{-1}$ at $k_x = -0.27$ Å$^{-1}$ is displayed in Figs. 11(b) and (c). Here, the spectra were obtained with an experimental setup that is sensitive to spins with $\vec{P}$ parallel to the [$\bar{1}$10] direction of Tl/Si(110)-(1×1), i.e. the $y$ direction in Fig. 11, and thus reveal that the upper bands are spin-polarized and that $\vec{P}$ principally points toward the $-y$ ($+y$) direction at $k_x < 0$ ($k_x > 0$).

$C_{1h}$ is a symmetry with one mirror plane only. Since the $\bar{\Gamma}$-$\bar{X}'$ line is on the mirror plane, not only the $\bar{\Gamma}$ and $\bar{X}'$ points but all the $\vec{k}$ points on this line have $C_{1h}$ symmetry. Taking into account that the spin components parallel to the mirror plane become zero and only the component normal to the mirror plane survives at $\vec{k}$ points with $C_{1h}$ symmetry [43], $\vec{P}$ is $P_y \neq 0$ and $P_x = P_z = 0$ at all $\vec{k}$ points on the $\bar{\Gamma}$-$\bar{X}'$ line in this system. This leads the two $k_y = 0$ points of each constant energy contour to have same sign of $P_y$ (minus for the constant energy contour at $k_x < 0$ and plus for the one at $k_x > 0$) because a $\vec{k}$ point with time-reversal symmetry is necessary to reverse the $\vec{P}$ of a RB band to the opposite direction. The presence of these two $\vec{k}$ points having the same $\vec{P}$ direction between $\bar{\Gamma}$ and $\bar{X}'$ locks the direction of $\vec{P}$ of a constant energy contour and therefore prevents the formation of a vortical spin structure. Furthermore, because the peculiar constant energy contour with its center at a $\vec{k}$ point with non time-reversal symmetry results from the lack of rotational symmetry, we conclude that the novel RB non-vortical spin structure observed on Tl/Si(110)-(1×1) is a consequence of the $C_{1h}$ symmetry of this system.

### *3.2. OAM induced spin-polarized bands*

We have discussed the relationship between the symmetry of the atomic structure and spin splitting. In this subsection, we will consider why the symmetry of the atomic structure is relevant to the spin structure. As shown in sub-subsection 3.1.1, the upstanding spin at a $\vec{k}$ point with $C_3$ symmetry results from the circular motion of electrons in the $xy$ plane. The effect of the

electron motion suggests that the OAM would play an important role for the spin-polarized bands on ALMs. In order to understand this point in more detail, we discuss the spin-polarized band of a Si(111) surface covered with 2 layers of In. As shown in Figs. 12(a) and (b), the adsorbed In bilayer forms a square lattice on the triangular Si lattice that leads to a $(\sqrt{7}\times\sqrt{3})$ reconstructed structure that has only a mirror plane along the $[11\bar{2}]$ direction and thus belongs to the $p1m1$ plane group. (This In/Si(111)-$(\sqrt{7}\times\sqrt{3})$ is known to have metallic surface states [95, 96] and to become superconducting below 3 K [97, 98].)

Figure 13(a) shows the experimentally obtained Fermi surface (FS) of In/Si(111)-$(\sqrt{7}\times\sqrt{3})$ together with theoretically obtained one. The complex shape of the experimental FS obtained from the summation of the photoelectron intensity within a 5 meV energy window from the Fermi level shows good agreement with that reported experimentally in a former study [95], but with clear splittings. That is, neither the small splitting at around the point labeled A in Fig. 13(a) nor the large splitting around the area B were observed in the former study. (In Ref. [95], the complex looking FS is reported to result from the backfolding of two metallic bands in the reduced Brillouin zone, i.e. a two-dimensional nearly-free-electron metallic band forming a circular FS and a band forming a small FS around the $\bar{X}$. This former study also reported that the FS of In/Si(111)-$(\sqrt{7}\times\sqrt{3})$ is mainly formed by the circular one.) Taking into account that the theoretical FS shows splitting only when including the SOC as shown in Fig. 14 and in [96, 99], we conclude that both the small splitting at around the point labeled A in Fig. 13(a) and the large one around the point B result from SOC. To simplify the discussion, we hereafter call the circular FS indicated by khaki lines in Fig. 13(a) as the "circular FS", and that indicated by dark khaki lines as" butterfly FS". The largest $\vec{k}_{||}$ splitting of the circular FS was 0.007 Å$^{-1}$ and that of the butterfly FS was 0.035 Å$^{-1}$.

The spin-resolved energy distribution curves in Fig. 13(b) indicate that the $y$ component mainly contributes to the $\vec{P}$ at the point A of the circular FS with a small contribution from the $x$ component, and the spin-resolved momentum distribution curves in Fig. 13(c) show that the main component of the $\vec{P}$ for

cut B of the butterfly FS is the $x$ component. Here, the $x$, $y$ and $z$ directions correspond to $[1\bar{1}0]$, $[11\bar{2}]$ and [111], respectively. The result in Fig. 13(b) implies the $\vec{P}$ to be tangential to the FS as expected for ordinary RB spins. In contrast to this RB spin structure, the $\vec{P}$ in (c) cannot be explained by a simple RB effect and even not by the symmetry induced RB effect since the $\vec{k}$ at cut B is a point without any rotational and mirror symmetries. The sign of the $x$ component of $\vec{P}$ flips when $k_y$ changes its sign. That is, the $\vec{P}$ of the inner butterfly points along the $-x$ direction at cut B with $k_y \sim -0.1$ Å$^{-1}$ and along the $+x$ direction at $k_y \sim +0.1$ Å$^{-1}$. Regarding the outer butterfly, it shows the opposite behavior, the $\vec{P}$ points along the $+x$ direction at $k_y \sim -0.1$ Å$^{-1}$ and along $-x$ at $k_y \sim +0.1$ Å$^{-1}$ as shown in Fig. 13(a). This spin flip at $k_y = 0$ results from the $C_{1h}$ symmetry with a mirror plane on the $[11\bar{2}]$ direction. That is, the time-reversal symmetry flips all the three $x$, $y$, and $z$ components of $\vec{P}$, while a mirror symmetry with a mirror plane in the $yz$ plane at $k_x = 0$ Å$^{-1}$ inverts only the $y$ and $z$ component of $\vec{P}$. This combination leads to the flip of only the $x$ component when changing $\vec{k}$ from $(k_x, k_y)$ to $(k_x, -k_y)$. This simple procedure is supported by the agreement with the theoretically obtained spin polarization shown in Fig. 14(a).

The spin texture shown in Fig. 14(a) can be explained by neither the Dresselhaus effect [100] nor the Zeeman effect. Since the circular motion of electrons and thus the OAM is a candidate of the origin of the spin splitting as mentioned above, we examined the OAM induced in In $5p$ shell when no SOC is included [101]. Figure 14(b) displays the obtained directions and size of the OAM on the FS. As shown in the figure, the directions of OAM show good correspondence with the $\vec{P}$ of not only the inner butterfly FS but also with that of the inner circular one. More detailed information on the correspondence can be obtained from Fig. 15, which shows the size and direction of OAM (c and f), the spin splitting in energy and the ratio between this splitting and the size of OAM (d and g) and the inner product of the OAM and $\vec{P}$ (e and h) at the $\vec{k}$ points of the circular FS labeled in (a) and those of the butterfly ones in (b). The size and direction cosine of OAM shown in Figs. 15(c) and (f) indicates that the OAM

points in the tangential direction with an almost constant size on the circular FS (Fig. 15(c)), and the OAM points in the perpendicular direction to the FS on the butterfly FS with a large variation in size (Fig. 15(f)). The inner product of the OAM and $\vec{P}$ shows values between 0.98 and 1.0, and therefore supports the good correspondence between the OAM and $\vec{P}$.

The effective magnetic field that is perpendicular to the plane of electron's circular motion lifts the spin degeneracy and consequently orients the $\vec{P}$ in the direction parallel or antiparallel to the OAM when the SOC is on. The parallel and antiparallel spins have different $E_B$, and thus split the band. The $E_B$ of the parallel spin is higher than that of the antiparallel one, and this agrees well with the results shown in Fig. 14 where the $\vec{P}$ of both the inner circular and butterfly FSs, whose $E_B$s are higher than those of the outer ones at a certain $\vec{k}$ point, is parallel to the OAM. Figures 15(d) and (g) display the spin splitting in $E_B$ together with the relation between the OAM size and energy splitting. The relation is obtained by the ratio between the energy splitting shown in Figs. 15(d) and (g) and the size of OAM in (c) and (f) as "Ratio=energy splitting (in eV)/OAM size (in $\hbar$)". The rather constant energy splitting/OAM size ratio of the circular FS, $\sim 1.45$, and the relatively constant ratio of the butterfly FS from the $\vec{k}$ point 1 to 9, $\sim 1.5$, are consistent with the SOC constant of In $5p$ state, 1.42 eV. The difference in ratio observed at the $\vec{k}$ point 2 of the circular FS, where the FS crosses the butterfly FS, and at the $\vec{k}$ point from 10 to 17 of the butterfly FS where the ratio is $\sim 1.1$, may result from factors ignored in the present analysis, such as higher-$l$ OAM. These results demonstrate that the primary origin of "both" spin-polarized states of In/Si(111)-($\sqrt{7}\times\sqrt{3}$) is OAM, and not the RB effect.

The OAM size of the circular FS is $\sim 0.06$, a value that is very close to that of the $\vec{k}$ point 6 of the butterfly FS, though the splitting in $\vec{k}$ is significantly different. The splitting is 0.007 Å$^{-1}$ at the $\vec{k}$ point 4 of the circular FS and 0.033 Å$^{-1}$ at the $\vec{k}$ point 6 of the butterfly FS. This difference is due to the fact that SOC induces a spin splitting along the energy direction, and the splitting along $\vec{k}$ is a result of this energy splitting. In other words, the splitting in $\vec{k}$ depends

on the gradient of the band dispersion. Comparing the dispersion of the bands forming the two FSs, one notices that the $E_B$ splittings at the $\vec{k}$ point 4 of the circular FS and the $\vec{k}$ point 6 of the butterfly FS are rather similar, and that the dispersion of the former one is much steeper than that of the latter one as shown in Fig. 16. (The gradient of the circular FS is ∼14.7 eV·Å in Fig. 16(a) and that of the butterfly FS is 2.8eV·Å in (b).)

## 4. Conclusion

In this article, we review the recent progress in the understanding of the origin of spin-polarized electronic states in 2D ALMs formed on solid surfaces. Based on photoelectron spectroscopy, inverse photoemission and DFT calculation, we first demonstrate that depending on the symmetry of the atomic structure of the ALM, the spin-polarized electronic states show behavior that differ from that of an ordinary RB effect. That is, $\vec{P}$ points along the surface normal direction at a $\vec{k}$ point with $C_3$ symmetry, $\vec{P}$ shows a RB-type spin splitting even at a $\vec{k}$ point without time-reversal symmetry though this was thought to be a necessary condition for the RB effect, and $\vec{P}$ shows a non-vortical spin structure in case of a system with $C_{1h}$ symmetry. The symmetry induced peculiar spin texture has a strong correlation with the electron motions as presented in sub-subsection 3.1.1, i.e. a $C_3$ symmetry causes a circular motion of electrons that leads the spin direction to be perpendicular to this motion. Taking into account that the effect of the electron motion suggests the OAM to play a significant role for the spin-polarized bands on ALMs, we next demonstrate the relation between spin-polarized bands and OAM of In/Si(111)-($\sqrt{7} \times \sqrt{3}$). Based on all the above results, we conclude that OAM induces various spin textures, ranging from the RB-type to a type that cannot be explained based on the RB effect but which depends on the distribution of the electron density, and that $\vec{P}$ is determined by the direction of OAM. Extension of the present model of OAM induced spin-polarized bands to other 2D atomic layers materials, such as AL superconductor, would be an exciting direction for future work for the

realization of novel spintronics and/or quantum devices, and for discussing novel physical properties such as the effect of SOC to superconducting states formed by 2D materials with spin- polarized electronic states [62, 102, 103].

**Acknowledgements**

The authors thanks Ayako, Imaki, Haruya Kakuta, Takuya Kuzumaki, Emilia Annese, Yuta Yamamoto, Beate Müllerr, Minoru Ohtaka, Takashi Aoki, Hirotaka Ishikawa, Takashi Hayashida and Yoshitaka Nakata of Chiba University Japan, Koji Miyamoto and Akio Kimura of Hiroshima University, Japan, Katsuaki Sugawara and Takashi Takahashi of Tohoku University, Japan, Yasuo Takeichi (now at KEK-PF, Japan), Ayumi Harasawa and Tetsuroh Shirasawa (now at AIST, Japan) of the University of Tokyo, Takashi Uchihashi, Shunsuke Yoshizawa and Kazushi Miki (now at University of Hyogo, Japan) of the National Institute for Materials Science, Japan, Tatsuki Oda of Kanazawa University, Japan, Tamio Oguchi of Osaka University, Sebastian D. Stolwijk and Anke B. Schmidt of Westfälische Wilhelms-Universität Münster, Germany, Tae-Hwan Kim and Han Woong Yeom of Pohang University of Science and Technology, Korea, R.I.G. Uhrberg of Linköping University, Sweden, and Daniel Agterberg and Michael Weinert of University of Wisconsin-Milwaukee, USA for the contributions in this project. This research is supported by the JSPS Grant-in-Aid for Scientific Research (A) JP20244045, JSPS Grant-in-Aid for Scientific Research (B) JP25287070 and JP19H02592, JSPS Grant-in-Aid for Scientific Research (C) 18K03484, the JSPS Grant-in-Aid for Specially Promoted Research JP20H05621, and the JSPS Grant-in-Aid for Scientific Research on Innovative Areas “3D Active-Site Science” JP17H05211 and “Nano-Material Optical-Manipulation” JP17H05461, and by the National Science Foundation, Grant No. EFMA-1741673.

## References

[1] P. Vogt, P. De Padova, C. Quaresima, J. Avila, E. Frantzeskakis, M. C. Asensio, A. Resta, B. Ealet, G. Le Lay, Silicene:

Compelling Experimental Evidence for Graphenelike Two-Dimensional Silicon, Phys. Rev. Lett. 108 (2012) 155501. doi:https://doi.org/10.1103/PhysRevLett.108.155501.

[2] G. Liu, S. B. Liu, B. Xu, C. Y. Ouyang, H. Y. Song, S. Guan, S. A. Yang, Multiple Dirac Points and Hydrogenation-Induced Magnetism of Germanene Layer on Al(111) Surface, J. Phys. Chem. Lett. 6 (2015) 4936. doi:https://doi.org/10.1021/acs.jpclett.5b02413.

[3] J. Yuhara, H. Shimazu, K. Ito, A. Ohta, M. Araidai, M. Kurosawa, M. Nakatake, G. L. Lay, Germanene Epitaxial Growth by Segregation through Ag(111) Thin Films on Ge(111), ACS Nano 12 (2018) 11632. doi:https://doi.org/10.1021/acsnano.8b07006.

[4] A. J. Mannix, X.-F. Zhou, B. Kiraly, J. D. Wood, D. Alducin, B. D. Myers, X. Liu, B. L. Fisher, U. Santiago, J. R. Guest, M. J. Yacaman, A. Ponce, A. R. Oganov, M. C. Hersam, N. P. Guisinger, Synthesis of borophenes: Anisotropic, two-dimensional boron polymorphs, Science 350 (2015) 1513. doi:https://doi.org/10.1126/science.aad1080.

[5] B. Feng, O. Sugino, R.-Y. Liu, J. Zhang, R. Yukawa, M. Kawamura, T. Iimori, H. Kim, Y. Hasegawa, H. Li, L. Chen, K. Wu, H. Kumigashira, F. Komori, T.-C. Chiang, S. Meng, I. Matsuda, Dirac Fermions in Borophene, Phys. Rev. Lett. 118 (2017) 096401. doi:https://doi.org/10.1103/PhysRevLett.118.096401.

[6] J.-F. Ge, Z.-L. Liu, C. Liu, C.-L. Gao, D. Qian, Q.-K. Xue, Y. Liu, J.-F. Jia, Superconductivity above 100 K in single-layer FeSe films on doped $SrTiO_3$, Nat. Mater. 14 (2015) 285–289. doi:http://dx.doi.org/10.1038/nmat4153.

[7] S. Datta, B. Das, Electronic analog of the electro-optic modulator, Appl. Phys. Lett. 56 (1990) 665–667. doi:https://doi.org/10.1063/1.102730.

[8] D. Hägele, M. Oestreich, W. W. Rühle, Spin transport in GaAs, Appl. Phys. Lett. 73 (1998) 1580–1582. doi:https://doi.org/10.1063/1.122210.

[9] J. M. Kikkawa, D. D. Awschalom, Lateral drag of spin coherence in gallium arsenide, Nature 397 (1999) 139–141. doi:https://doi.org/10.1038/16420.

[10] S. A. Wolf, D. D. Awschalom, R. A. Buhrman, J. M. Daughton, S. v. Molnàr, M. L. Roukes, A. Y. Chtchelkanove, D. M. Treger, Spintronics: A Spin-Based Electronics Vision for the Future, Science 294 (2001) 1488–1495. doi:https://doi.org/10.1126/science.1065389.

[11] I. Zŭtić, J. Fabian, S. Das Sarma, Spintronics: fundamentals and applications, Rev. Mod. Phys. 76 (2004) 323–410. doi:https://doi.org/10.1103/RevModPhys.76.323.

[12] D. D. Aswchalom, M. E. Flatté, Challenges for semiconductor spintronics, Nat. Phys. 3 (2007) 153–159. doi:https://doi.org/10.1038/nphys551.

[13] S. Nadj-Perge, S. M. Frolov, E. P. A. M. Bakkers, L. P. Kouwenhoven, Spin-orbit qubit in a semiconductor nanowire, Nature 468 (2010) 1084–1087. doi:https://doi.org/10.1038/nature09682.

[14] Y. A. Bychkov, E. I. Rashba, Properties of a 2D electron gas with lifted spectral degeneracy, JETP Lett. 39 (1984) 78.

[15] S. LaShell, B. A. McDougall, E. Jensen, Spin Splitting of an Au(111) Surface State Band Observed with Angle Resolved Photoelectron Spectroscopy, Phys. Rev. Lett. 77 (1996) 3419–3422. doi:https://doi.org/10.1103/PhysRevLett.77.3419.

[16] G. Nicolay, F. Reinert, S. Hüfner, P. Blaha, Spin-orbit splitting of the L-gap surface state on Au(111) and Ag(111), Phys. Rev. B 65 (2001) 033407. doi:https://doi.org/10.1103/PhysRevB.65.033407.

[17] F. Reinert, Spin-orbit interaction in the photoemission spectra of noble metal surface states, J. Phys. Condens. Matter. 15 (2003) S693–S705. doi:https://doi.org/10.1088/0953-8984/15/5/321.

[18] J. Henk, A. Ernst, P. Bruno, Spin polarization of the L-gap surface states on Au(111): a first-principles investigation, Surf. Sci. 566-568 (2004) 482–485. doi:https://doi.org/10.1016/j.susc.2004.05.088.

[19] J. Henk, M. Hoesch, J. Osterwalder, A. Ernst, P. Bruno, Spin-orbit coupling in the L-gap surface states of Au(111): spin-resolved photoemission experiments and first-principles calculations, J. Phys. Condens. Matter. 16 (2004) 7581–7597. doi:https://doi.org/10.1088/0953-8984/16/43/002.

[20] M. Hoesch, M. Muntwiler, V. N. Petrov, M. Hengsberger, L. Patthey, M. Shi, M. Falub, T. Greber, J. Osterwalder, Spin structure of the Shockley surface state on Au(111), Phys. Rev. B 69 (2004) 241401(R). doi:https://doi.org/10.1103/PhysRevB.69.241401.

[21] S. N. P. Wissing, C. Eibl, A. Zumbülte, A. B. Schmidt, J. Braun, J. Minár, H. Ebert, M. Donath, Rashba-type spin splitting at Au(111) beyond the Fermi level: the other part of the story, New J. Phys. 15 (2013) 105001. doi:https://doi.org/10.1088/1367-2630/15/10/105001.

[22] K. Yaji, A. Harasawa, K. Kuroda, R. Li, B. Yan, F. Komori, S. Shin, Rashba spin splitting of L-gap surface states on Ag(111) and Cu(111), Phys. Rev. B 98 (2018) 041404(R). doi:https://doi.org/10.1103/PhysRevB.98.041404.

[23] K. Yaji, Y. Ohtsubo, S. Hatta, H. Okuyama, K. Miyamoto, T. Okuda, A. Kimura, H. Namatame, M. Taniguchi, T. Aruga, Large Rashba spin splitting of a metallic surface-state band on a semiconductor surface, Nat. Commun. 1 (2010) 17. doi:https://doi.org/10.1038/ncomms1016.

[24] C. R. Ast, J. Henk, A. Ernst, L. Moreschini, M. C. Falub, D. Pacilé, P. Bruno, K. Kern, M. Grioni, Giant Spin Splitting through Surface Alloying, Phys. Rev. Lett. 98 (2007) 186807. doi:https://doi.org/10.1103/PhysRevLett.98.186807.

[25] S. N. P. Wissing, A. B. Schmidt, H. Mirhosseini, J. Henk, C. R. Ast, M. Donath, Ambiguity of Experimental Spin information from States with Mixed Orbital Symmetries, Phys. Rev. Lett. 113 (2014) 116402. doi:https://doi.org/10.1103/PhysRevLett.113.116402.

[26] M. Ünzelmann, H. Bentmann, P. Eck, T. Kißlinger, B. Geldiyev, J. Rieger, S. Moser, R. C. Vidal, K. Kißner, L. Hammer, M. A. Schneider, T. Fauster, G. Sangiovanni, D. Di Sante, F. Reinert, Orbital-Driven Rashba Effect in a Binary Honeycomb Monolayer AgTe, Phys. Rev. Lett. 124 (2020) 176401. doi:https://doi.org/10.1103/PhysRevLett.124.176401.

[27] M. Nagano, A. Kodama, T. Shishidou, T. Oguchi, A first-principles study on the Rashba effect in surface systems, J. Phys.: Condens. Matter. 21 (2009) 064239. doi:https://doi.org/10.1088/0953-8984/21/6/064239.

[28] K. Sakamoto, T. Oda, A. Kimura, K. Miyamoto, M. Tsujikawa, A. Imai, N. Ueno, H. Namatame, M. Taniguchi, P. E. J. Eriksson, R. I. G. Uhrberg, Abrupt Rotation of the Rashba Spin to the Direction Perpendicular to the Surface, Phys. Rev. Lett. 102 (2009) 096805. doi:https://doi.org/10.1103/PhysRevLett.102.096805.

[29] K. Sakamoto, H. Kakuta, K. Sugawara, K. Miyamoto, A. Kimura, T. Kuzumaki, N. Ueno, E. Annese, J. Fujii, A. Kodama, T. Shishidou, H. Namatame, M. Taniguchi, T. Sato, T. Takahashi, T. Oguchi, Peculiar Rashba Splitting Originating from the Two-Dimensional Symmetry of the Surface, Phys. Rev. Lett. 103 (2009) 156801. doi:https://doi.org/10.1103/PhysRevLett.103.156801.

[30] P. Höpfner, J. Schäfer, A. Fleszar, J. H. Dil, B. Slomski, F. Meier, C. Loho, C. Blumenstein, L. Patthey, W. Hanke, R. Claessen, Three-Dimensional Spin Rotations at the Fermi Surface of a Strongly Spin-Orbit Coupled Surface System, Phys. Rev. Lett. 108 (2012) 186801. doi:https://doi.org/10.1103/PhysRevLett.108.186801.

[31] Y. Ohtsubo, S. Hatta, H. Okuyama, T. Aruga, A metallic surface state with uniaxial spin polarization on Tl/Ge(111)-(1×1), J. Phys.: Condens. Matter 24 (2012) 092001. doi:https://doi.org/10.1088/0953-8984/24/9/092001.

[32] K. Sakamoto, T.-H. Kim, T. Kuzumaki, B. Müller, Y. Yamamoto, M. Ohtaka, J. R. Osiecki, K. Miyamoto, Y. Takeichi, A. Harasawa, S. D. Stolwijk, A. B. Schmidt, J. Fujii, R. I. G. Uhrberg, M. Donath, H. W. Yeom, T. Oda, Valley spin polarization by using the extraordinary Rashba effect on silicon, Nat. Commun. 4 (2013) 2073. doi:https://doi.org/10.1038/ncomms3073.

[33] S. D. Stolwijk, A. B. Schmidt, M. Donath, K. Sakamoto, P. Krüger, Rotating Spin and Giant Splitting: Unoccupied Surface Electronic Structure of Tl/Si(111), Phys. Rev. Lett. 111 (2013) 176402. doi:https://doi.org/10.1103/PhysRevLett.111.176402.

[34] K. Nakajin, S. Murakami, Theory of unconventional spin states in surfaces with non-Rashba spin-orbit interaction, Phys. Rev. B 91 (2015) 245428. doi:https://doi.org/10.1103/PhysRevB.91.245428.

[35] E. Annese, T. Kuzumaki, B. Müller, Y. Yamamoto, H. Nakano, H. Kato, A. Araki, M. Ohtaka, T. Aoki, H. Ishikawa, T. Hayashida, J. R. Osiecki, K. Miyamoto, Y. Takeichi, A. Harasawa, K. Yaji, T. Shirasawa, K.-i. Nittoh, W. Yang, K. Miki, T. Oda, H. W. Yeom, K. Sakamoto, Nonvortical Rashba Spin Structure on a Surface with C1h Symmetry, Phys. Rev. Lett. 117 (2016) 016803. doi:https://doi.org/10.1103/PhysRevLett.117.016803.

[36] P. Eickholt, P. Krüger, S. D. Stolwijk, A. B. Schmidt, M. Donath, Effects of orbital composition in a pair of spin-orbit-split surface bands at Tl/Ge(111), Phys. Rev. B 93 (2016) 085412. doi:https://doi.org/10.1103/PhysRevB.93.085412.

[37] C. Brand, S. Muff, M. Fanciulli, H. Pfnür, M. C. Tringides, J. H. Dil, C. Tegenkamp, Spin-resolved band structure of a densely packed Pb monolayer on Si(111), Phys. Rev. B 96 (2017) 035432. doi:https://doi.org/10.1103/PhysRevB.96.035432.

[38] R. Noguchi, K. Kuroda, K. Yaji, K. Kobayashi, M. Sakano, A. Harasawa, T. Kondo, F. Komori, S. Shin, Direct mapping of spin and orbital entangled wave functions under interband spin-orbit coupling of giant Rashba spin-split surface states, Phys. Rev. B 95 (2017) 041111(R). doi:https://doi.org/10.1103/PhysRevB.95.041111.

[39] K. Yaji, A. Visikovskiy, T. Iimori, K. Kuroda, S. Hayashi, T. Kajiwara, S. Tanaka, F. Komori, S. Shin, Coexistence of Two Types of Spin Splitting Originating from Different Symmetries, Phys. Rev. Lett. 122 (2019) 126403. doi:https://doi.org/10.1103/PhysRevLett.122.126403.

[40] T. Kobayashi, Y. Nakata, K. Yaji, T. Shishidou, D. Agterberg, S. Yoshizawa, F. Komori, S. Shin, M. Weinert, T. Uchihashi, K. Sakamoto, Orbital Angular Momentum Induced Spin Polarization of 2D Metallic Bands, Phys. Rev. Lett. 125 (2020) 176401. doi:https://doi.org/10.1103/PhysRevLett.125.176401.

[41] S. R. Park, C. H. Kim, J. Yu, J. H. Han, C. Kim, Orbital-Angular-Momentum Based Origin of Rashba-Type Surface Band Splitting, Phys. Rev. Lett. 107 (2011) 156803. doi:https://doi.org/10.1103/PhysRevLett.107.156803.

[42] D. Go, J.-P. Hanke, P. M. Buhl, F. Freimuth, G. Bihlmayer, H.-W. Lee, Y. Mokrousov, S. Blügel, Toward surface orbitronics: giant orbital mag-

netism from the orbital Rashba effect at the surface of sp-metals, Sci. Rep. 7 (2017) 46742. doi:https://doi.org/10.1038/srep46742.

[43] T. Oguchi, T. Shishidou, The surface Rashba effect: a k-p perturbation approach, J. Phys.: Condens. Matter 21 (2009) 092001. doi:https://doi.org/10.1088/0953-8984/21/9/092001.

[44] D. Popović, F. Reinert, S. Hüfner, V. G. Grigoryan, M. Springborg, H. Cercellier, Y. Fagot-Revurat, B. Kierren, D. Malterre, High-resolution photoemission on Ag/Au(111): Spin-orbit splitting and electronic localization of the surface state, Phys. Rev. B 72 (2005) 045419. doi:https://doi.org/10.1103/PhysRevB.72.045419.

[45] H. Cercellier, C. Didiot, Y. Fagot-Revurat, B. Kierren, L. Moreau, D. Malterre, F. Reinert, Interplay between structural, chemical, and spectroscopic properties of Ag/Au(111) epitaxial ultrathin films: A way to tune the Rashba coupling, Phys. Rev. B 73 (2006) 195413. doi:https://doi.org/10.1103/PhysRevB.73.195413.

[46] D. Malterre, B. Kierren, Y. Fagot-Revurat, S. Pons, A. Tejeda, C. Didiot, H. Cercellier, A. Bendounan, ARPES and STS investigation of Shockley states in thin metallic films and periodic nanostructures, New J. Phys. 9 (2007) 391. doi:https://doi.org/10.1088/1367-2630/9/10/391.

[47] Y. M. Koroteev, G. Bihlmayer, J. E. Gayone, E. V. Chulkov, S. Blügel, P. M. Echenique, P. Hofmann, Strong Spin-Orbit Splitting on Bi Surfaces, Phys. Rev. Lett. 93 (2004) 046403. doi:https://doi.org/10.1103/PhysRevLett.93.046403.

[48] K. Sugawara, T. Sato, S. Souma, T. Takahashi, M. Arai, T. Sasaki, Fermi Surface and Anisotropic Spin-Orbit Coupling of Sb(111) Studied by Angle-Resolved Photoemission Spectroscopy, Phys. Rev. Lett. 96 (2006) 046411. doi:https://doi.org/10.1103/PhysRevLett.96.046411.

[49] T. Hirahara, T. Nagao, I. Matsuda, G. Bihlmayer, E. V. Chulkov, Y. M. Koroteev, P. M. Echenique, M. Saito, S. Hasegawa, Role of Spin-Orbit Coupling and Hybridization Effects in the Electronic Structure of Ultrathin Bi Films, Phys. Rev. Lett. 97 (2006) 146803. doi:https://doi.org/10.1103/PhysRevLett.97.146803.

[50] I. Gierz, T. Suzuki, E. Frantzeskakis, S. Pons, S. Ostanin, A. Ernst, J. Henk, M. Grioni, K. Kern, C. R. Ast, Silicon Surface with Giant Spin Splitting, Phys. Rev. Lett. 103 (2009) 046803. doi:https://doi.org/10.1103/PhysRevLett.103.046803.

[51] A. Takayama, T. Sato, S. Souma, T. Takahashi, Giant Out-of-Plane Spin Component and the Asymmetry of Spin Polarization in Surface Rashba States of Bismuth Thin Film, Phys. Rev. Lett. 106 (2011) 166401. doi:https://doi.org/10.1103/PhysRevLett.106.166401.

[52] B. Slomski, G. Landolt, F. Meier, L. Patthey, G. Bihlmayer, J. Osterwalder, J. H. Dil, Manipulating the Rashba-type spin splitting and spin texture of Pb quantum well states, Phys. Rev. B 84 (2011) 193406. doi:https://doi.org/10.1103/PhysRevB.84.193406.

[53] S. D. Stolwijk, K. Sakamoto, A. B. Schmidt, P. Krüger, M. Donath, Thin line of a Rashba-type spin texture: Unoccupied surface resonance of Tl/Si(111) along $\bar{\Gamma}\bar{M}$, Phys. Rev. B 90 (2014) 161109(R). doi:https://doi.org/10.1103/PhysRevB.90.161109.

[54] R. Suzuki, M. Sakano, Y. J. Zhang, R. Akashi, D. Morikawa, A. Harasawa, K. Yaji, K. Kuroda, K. Miyamoto, T. Okuda, K. Ishizaka, R. Arita, Y. Iwasa, Valley-dependent spin polarization in bulk $MoS_2$ with broken inversion symmetry, Nat. Nanotechnol. 9 (2014) 611–617. doi:https://doi.org/10.1038/nnano.2014.148.

[55] S. D. Stolwijk, K. Sakamoto, A. B. Schmidt, P. Krüger, M. Donath, Spin texture with a twist in momentum space for Tl/Si(111), Phys. Rev. B 91 (2015) 245420. doi:https://doi.org/10.1103/PhysRevB.91.245420.

[56] B. Pieczyrak, M. Szary, L. Jurczyszyn, M. W. Radny, Spin polarization of two-dimensional electronic gas decoupled from structural asymmetry environment, Phys. Rev. B 93 (2016) 195318. doi:https://doi.org/10.1103/PhysRevB.93.195318.

[57] S. D. Stolwijk, A. B. Schmidt, K. Sakamoto, P. Krüger, M. Donath, Valley spin polarization of Tl/Si(111), Phys. Rev. Materials 1 (2017) 064604. doi:https://doi.org/10.1103/PhysRevMaterials.1.064604.

[58] K. Miyamoto, H. Miyahara, K. Kuroda, T. Maegawa, A. Kimura, T. Okuda, Peculiar Rashba spin texture induced by C3v symmetry on the Bi(111) surface revisited, Phys. Rev. B 97 (2018) 085433. doi:https://doi.org/10.1103/PhysRevB.97.085433.

[59] K. Miyamoto, H. Wortelen, T. Okuda, J. Henk, M. Donath, Circular-polarized-light-induced spin polarization characterized for the Dirac-cone surface state at W(110) with C2v symmetry, Sci. Rep. 8 (2018) 10440. doi:https://doi.org/10.1038/s41598-018-28693-3.

[60] Y. Ohtsubo, Y. Yamashita, K. Hagiwara, S.-i. Ideta, K. Tanaka, R. Yukawa, K. Horiba, H. Kumigashira, K. Miyamoto, T. Okuda, W. Hirano, F. Iga, S.-i. Kimura, Non-trivial surface states of samarium hexaboride at the (111) surface, Nat. Commun. 10 (2019) 2298. doi:https://doi.org/10.1038/s41467-019-10353-3.

[61] J. D. Sau, R. M. Lutchyn, S. Tewari, S. D. Sarma, Generic New Platform for Topological Quantum Computation Using Semiconductor Heterostructures, Phys. Rev. Lett. 104 (2010) 040502. doi:https://doi.org/10.1103/PhysRevLett.104.040502.

[62] M. Smidman, M. B. Salamon, H. Q. Yuan, D. F. Agterberg, Superconductivity and spin-orbit coupling in non-centrosymmetric materials: a review, Rep. Prog. Phys. 80 (2017) 036501. doi:https://doi.org/10.1088/1361-6633/80/3/036501.

[63] C. Lei, H. Chen, A. H. MacDonald, Ultrathin Films of Superconducting Metals as a Platform for Topological Superconductivity, Phys. Rev. Lett. 121 (2018) 227701. doi:https://doi.org/10.1103/PhysRevLett.121.227701.

[64] M. Budke, T. Allmers, M. Donath, G. Rangelov, Combined experimental setup for spin- and angle-resolved direct and inverse photoemission, Rev. Sci. Instrum. 78 (2007) 113909. doi:https://doi.org/10.1063/1.2813345.

[65] S. D. Stolwijk, H. Wortelen, A. B. Schmidt, M. Donath, Rotatable spin-polarized electron source for inverse-photoemission experiments, Rev. Sci. Instrum. 85 (2014) 013306. doi:https://doi.org/10.1063/1.4863097.

[66] M. Budke, V. Renken, Inverse photoemission with energy resolution better than 200 mev, Rev. Sci. Instrum. 78 (2007) 083903. doi:https://doi.org/10.1063/1.2771096.

[67] S. D. Stolwijk, Spin-orbit-induced spin textures of unoccupied surface states on Tl/Si(111), Springer Theses, Springer, 2015.

[68] A. Zumbülte, A. B. Schmidt, M. Donath, Momentum resolution in inverse photoemission, Rev. Sci. Instrum. 85 (2015) 013908. doi:https://doi.org/10.1063/1.4906508.

[69] A. Zumbülte, A. B. Schmidt, M. Donath, Erratum: "Momentum resolution in inverse photoemission" [Rev. Sci. Instrum. 86, 013908 (2015)], Rev. Sci. Instrum. 86 (2015) 069901. doi:https://doi.org/10.1063/1.4923090.

[70] J. Viernow, J.-L. Lin, D. Y. Petrovykh, F. M. Leibsle, F. K. Men, F. J. Himpsel, Regular step arrays on silicon, Appl. Phys. Lett. 72 (1998) 948–950. doi:https://doi.org/10.1063/1.120882.

[71] J.-L. Lin, D. Y. Petrovykh, J. Viernow, F. K. Men, D. J. Seo, F. J. Himpsel, Formation of regular step arrays on Si(111)7×7, J. Appl. Phys. 84 (1998) 255–260. doi:https://doi.org/10.1063/1.368077.

[72] J. P. Perdew, J. A. Chevary, S. H. Vosko, K. A. Jackson, M. R. Pederson, D. J. Singh, C. Fiolhais, Atoms, molecules, solids, and surfaces: Applications of the generalized gradient approximation for exchange and correlation, Phys. Rev. B 46 (1993) 6671–6687. doi:https://doi.org/10.1103/PhysRevB.46.6671.

[73] P. Hohenberg, W. Kohn, Inhomogeneous Electron Gas, Phys. Rev. 136 (1964) B864–B871. doi:https://doi.org/10.1103/PhysRev.136.B864.

[74] D. Vanderbilt, Soft self-consistent pseudopotentials in a generalized eigenvalue formalism, Phys. Rev. B 41 (1990) 7892(R)–7895(R). doi:https://doi.org/10.1103/PhysRevB.41.7892.

[75] K. Laasonen, A. Pasquarello, R. Car, C. Lee, D. Vanderbilt, Car-Parrinello molecular dynamics with vanderbilt ultrasoft pseudopotentials, Phys. Rev. B 47 (1993) 10142–10153. doi:https://doi.org/10.1103/PhysRevB.47.10142.

[76] M. Weinert, G. Schneider, R. Podloucky, J. Redinger, FLAPW: applications and implementations, J. Phys.: Condens. Matter. 21 (2009) 084201. doi:https://doi.org/10.1088/0953-8984/21/8/084201.

[77] S. S. Lee, H. J. Song, N. D. Kim, J. W. Chung, K. Kong, D. Ahn, H. Yi, B. D. Yu, H. Tochihara, Structural and electronic properties of thallium overlayers on the Si(111)7×7 surface, Phys. Rev. B 66 (2002) 233312. doi:https://doi.org/10.1103/PhysRevB.66.233312.

[78] K. Sakamoto, P. E. J. Eriksson, S. Mizuno, N. Ueno, H. Tochihara, R. I. G. Uhrberg, Core-level photoemission study of thallium adsorbed on a Si(111)-(7×7) surface: Valence state of thallium and

the charge state of surface Si atoms, Phys. Rev. B 74 (2006) 075335. doi:https://doi.org/10.1103/PhysRevB.74.075335.

[79] H. Wortelen, H. Mirhosseini, K. Miyamoto, A. B. Schmidt, J. Henk, M. Donath, Tuning the spin signal from a highly symmetric unpolarized electronic state, Phys. Rev. B 91 (2015) 115420. doi:https://doi.org/10.1103/PhysRevB.91.115420.

[80] J. Henk, K. Miyamoto, M. Donath, Retrieving the initial-state spin polarization from spin-resolved photoemission: Proposal for a case study on W(110), Phys. Rev. B 98 (2018) 045124. doi:https://doi.org/10.1103/PhysRevB.98.045124.

[81] D. Soriano, F. Muñoz Rojas, J. Fernández-Rossier, J. J. Palacios, Hydrogenated graphene nanoribbons for spintronics, Phys. Rev. B 81 (2010) 165409. doi:https://doi.org/10.1103/PhysRevB.81.165409.

[82] D. Gunlycke, C. T. White, Graphene Valley Filter Using a Line Defect, Phys. Rev. Lett. 106 (2011) 136806. doi:https://doi.org/10.1103/PhysRevLett.106.136806.

[83] K. J. Wan, T. Guo, W. K. Ford, J. C. Hermanson, Initial growth of Bi films on a Si(111) substrate: Two phases of $\sqrt{3} \times \sqrt{3}$ low-energy-electron-diffraction pattern and their geometric structures, Phys. Rev. B 44 (1991) 3471(R)–3474(R). doi:https://doi.org/10.1103/PhysRevB.44.3471.

[84] K. J. Wan, T. Guo, W. K. Ford, J. C. Hermanson, Low-energy electron diffraction studies of Si(111)-($\sqrt{3} \times \sqrt{3}$)R30°-Bi system: Observation and structural determination of two phases, Surf. Sci. 261 (1992) 69–87. doi:https://doi.org/10.1016/0039-6028(92)90219-V.

[85] T. Kuzumaki, T. Shirasawa, S. Mizuno, N. Ueno, H. Toshihara, K. Sakamoto, Re-investigation of the Bi-induced Si(111)-($\sqrt{3} \times \sqrt{3}$) surfaces by low-energy electron diffraction, Surf. Sci. 604 (2010) 1044–1048. doi:https://doi.org/10.1016/j.susc.2010.03.022.

[86] L. C. Snyder, Z. Wasserman, J. W. Moskowitz, Milk - stool model for Si(111) surface reconstruction, J. Vacuum Sci. Technol. 16 (1979) 1266. doi:https://doi.org/10.1116/1.570139.

[87] T. Kinoshita, S. Kono, H. Nagayoshi, Angle-Resolved Ultraviolet Photoelectron Spectroscopy Study of the Si(111)$\sqrt{3} \times \sqrt{3}$-Bi Surface, J. Phys. Soc. Jpn. 56 (1987) 2511–2515. doi:https://doi.org/10.1143/JPSJ.56.2511.

[88] Y. Kim, J.-S. Kim, C.-C. Hwang, S. P. Shrestha, K.-S. An, C.-Y. Park, Electronic Structure of the $\beta-$ Si(111) $\sqrt{3}\times\sqrt{3}-$ Bi Surface, J. Kor. Phys Soc. 39 (2001) 1032–1035.

[89] P. Roushan, J. Seo, C. V. Parker, Y. S. Hor, D. Hsieh, D. Qian, A. Richardella, M. Z. Hasan, R. J. Cava, A. Yazdani, Topological surface states protected from backscattering by chiral spin texture, Nature 460 (2009) 1106–1109. doi:https://doi.org/10.1038/nature08308.

[90] T. An, M. Yoshimura, I. Ono, K. Ueda, Elemental structure in Si(110)-"16×2" revealed by scanning tunneling microscopy, Phys. Rev. B 61 (2000) 3006–3011. doi:https://doi.org/10.1103/PhysRevB.61.3006.

[91] A. A. Stekolnikov, J. Furthmüller, F. Bechstedt, Long-Range Surface Reconstruction: Si(110)-(16×2), Phys. Rev. Lett. 93 (2004) 136104. doi:https://doi.org/10.1103/PhysRevLett.93.136104.

[92] A. A. Stekolnikov, J. Furthmüller, F. Bechstedt, Structural elements on reconstructed Si and Ge(110) surfaces, Phys. Rev. B 70 (2004) 045305. doi:https://doi.org/10.1103/PhysRevB.70.045305.

[93] K. Sakamoto, M. Setvin, K. Mawatari, P. E. J. Eriksson, K. Miki, R. I. G. Uhrberg, Electronic structure of the Si(110)-(16×2) surface: High-resolution ARPES and STM investigation, Phys. Rev. B 79 (2009) 045304. doi:https://doi.org/10.1103/PhysRevB.79.045304.

[94] T. Yamamoto, R. Izumi, K. Miki, T. Yamasaki, Y. Sugawara, Y. J. Li, Direct observation of the Si(110)-(16×2) surface reconstruction by atomic force microscopy, Beilstein J. Nanotechnol. 11 (2020) 1750–1756. doi:https://doi.org/10.3762/bjnano.11.157.

[95] E. Rotenberg, H. Koh, K. Rossnagel, H. W. Yeom, J. Schäfer, B. Krenzer, M. P. Rocha, S. D. Kevan, Indium $\sqrt{7} \times \sqrt{3}$ on Si(111): A Nearly Free Electron Metal in Two Dimensions, Phys. Rev. Lett. 91 (2003) 246404. doi:https://doi.org/10.1103/PhysRevLett.91.246404.

[96] K. Uchida, A. Oshiyama, Identification of metallic phases of In atomic layers on Si(111) surfaces, Phys. Rev. B 87 (2013) 165433. doi:https://doi.org/10.1103/PhysRevB.87.165433.

[97] T. Zhang, P. Cheng, W.-J. Li, Y.-J. Sun, G. Wang, X.-G. Zhu, K. He, L. Wang, X. Ma, X. Chen, Y. Wang, Y. Liu, H.-Q. Lin, J.-F. Jia, Q.-K. Xue, Superconductivity in one-atomic-layer metal films grown on Si(111), Nat. Phys. 6 (2010) 104. doi:https://doi.org/10.1038/nphys1499.

[98] T. Uchihashi, P. Mishra, M. Aono, T. Nakayama, Macroscopic Superconducting Current through a Silicon Surface Reconstruction with Indium Adatoms: Si(111)-($\sqrt{7} \times \sqrt{3}$)-In, Phys. Rev. Lett. 107 (2011) 207001. doi:https://doi.org/10.1103/PhysRevLett.107.207001.

[99] S. Yoshizawa, T. Kobayashi, Y. Nakata, K. Yaji, K. Yokota, F. Komori, S. Shin, K. Sakamoto, T. Uchihashi, Atomic-layer Rashba-type superconductor protected by dynamic spin-momentum locking, Nat. Commun. 12 (2021) 1462. doi:https://doi.org/10.1038/s41467-021-21642-1.

[100] G. Dresselhaus, Spin-Orbit Coupling Effects in Zinc Blende Structures, Phys. Rev. 100 (1955) 580–586. doi:https://doi.org/10.1103/PhysRev.100.580.

[101] S. Oh, H. J. Choi, Orbital angular momentum analysis for giant

spin splitting in solids and nanostructures, Sci. Rep. 7 (2017) 2024. doi:https://doi.org/10.1038/s41598-017-02032-4.

[102] D. F. Agterberg, J. C. Séamus Davis, S. D. Edkins, E. Fradkin, D. J. Van Harlingen, S. A. Kivelson, P. A. Lee, L. Radzihovsky, J. M. Tranquada, Y. Wang, The Physics of Pair-Density Waves: Cuprate Superconductors and Beyond, Annu. Rev. Condens. Matter Phys. 11 (2020) 231–270. doi:https://doi.org/10.1146/annurev-conmatphys-031119-050711.

[103] W.-Y. He, K. T. Law, Magnetoelectric effects in gyrotropic superconductors, Phys. Rev. Research 2 (2020) 012073(R). doi:https://doi.org/10.1103/PhysRevResearch.2.012073.

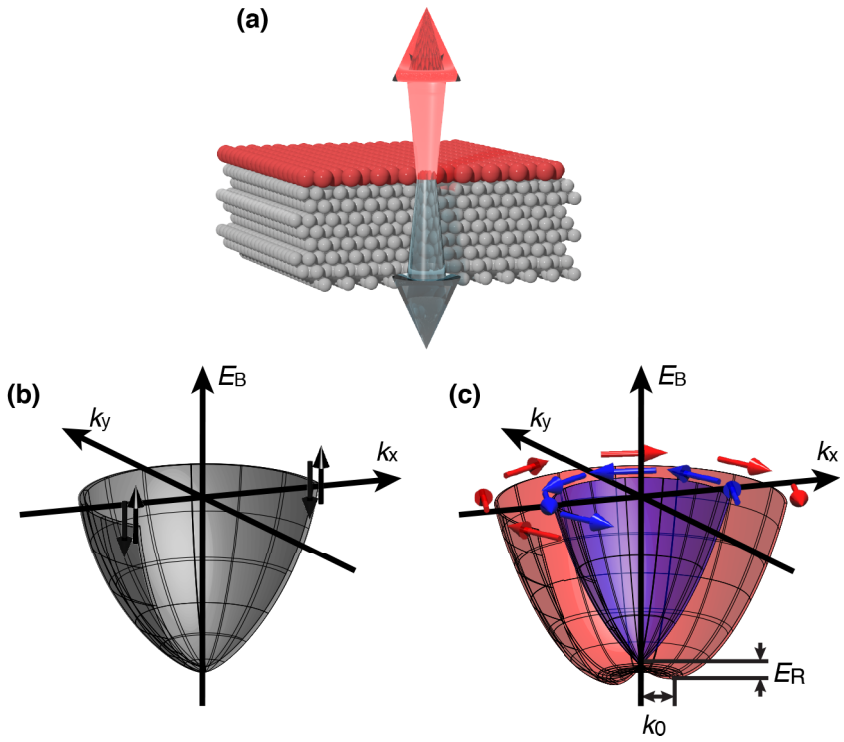


Figure 1: Schematic illustrations of (a) a single ALM formed on solid surface. The spatial inversion symmetry along the surface normal direction is broken due to the presence of the substrate in only one side. The arrows in (a) denotes the asymmetric spatial inversion along the surface normal direction. (b) Spin degenerated band structures of a non-magnetic 2D electron gas with both time-reversal and spatial inversion symmetries, and (c) spin split band structure arising from the RB effect.

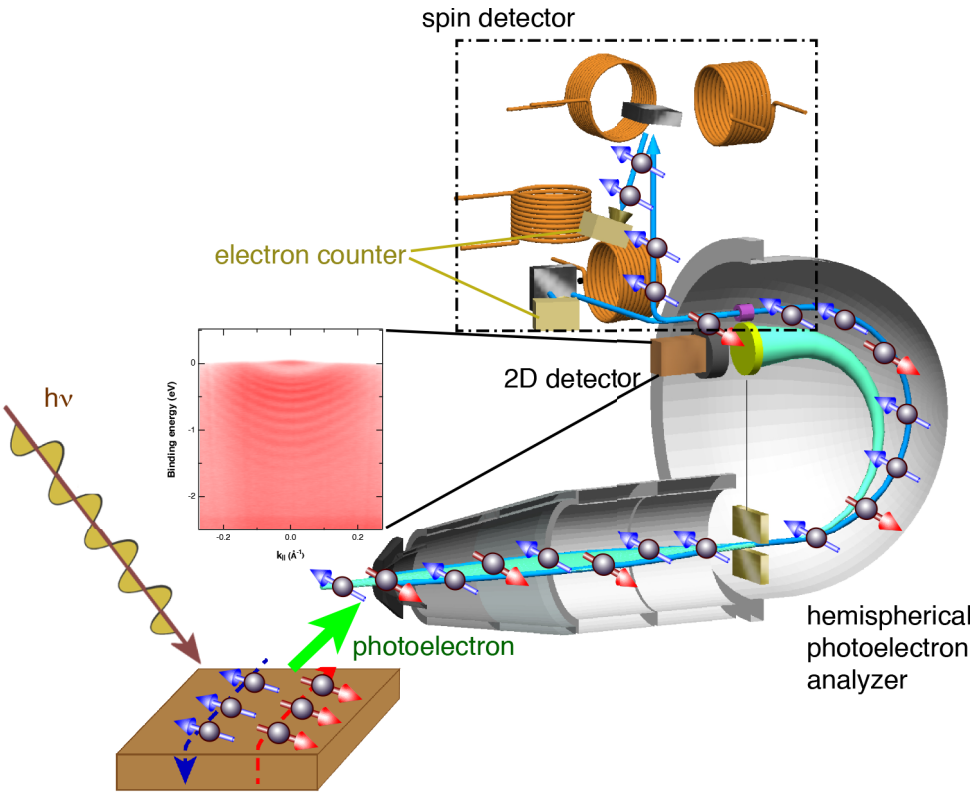


Figure 2: Schematic illustrations of ARPES and SARPES measurements. Photoelectrons, which are emitted from the sample, pass through the hemispherical analyzer and goes straight to the 2D detector for the ARPES measurements. Regarding the SARPES measurements, the trajectory of photoelectrons passed through the analyzer is bent by 90 degrees and guided to the spin detector. Usually, there are four electron counters in the spin detector (only two are shown in the figure to prevent cluttering) to allow us to obtained information about the $x$, $y$ and $z$ components of the electron spin polarization.

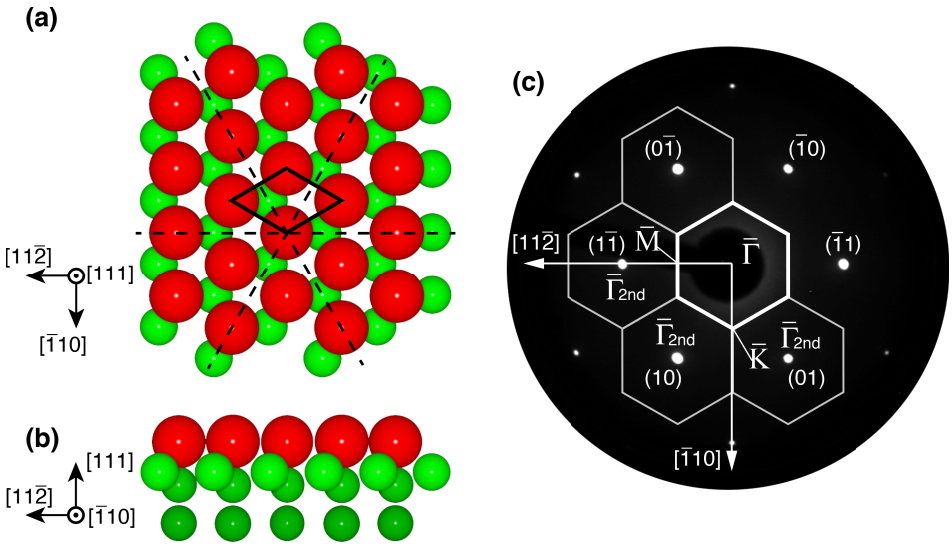


Figure 3: (a) Top view and (b) side view of Tl/Si(111)-(1×1). Red and green circles indicate the Tl and Si atoms, respectively. The diamond shape and dashed lines represent the (1×1) unit cell and the three mirror planes. (c) The LEED pattern, obtained with a primary electron energy of 104 eV, and the Brillouin zone of Tl/Si(111)-(1×1). The bold hexagon represents the first Brillouin zone and the thin ones are the second Brillouin zones. $\bar{\Gamma}$, $\bar{M}$, and $\bar{K}$ are the symmetry points of the (1×1) Brillouin zone.

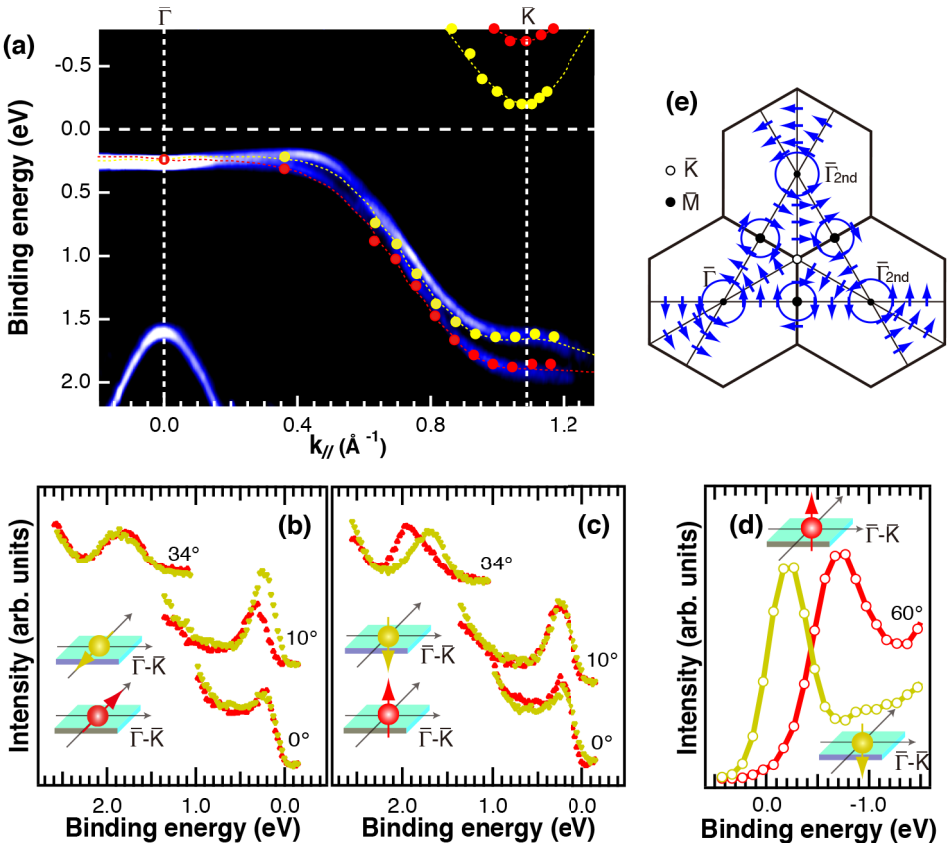


Figure 4: (a) Band structure of Tl/Si(111)-(1×1) obtained by ARPES and SARIPE. The dotted lines overlapping the experimentally obtained ARPES data are the theoretically band structure, and the circles overlapping these bands indicate the positions of spin-polarized peaks obtained experimentally. SARPES spectra at the $\bar{\Gamma}$ point ($\theta_e = 0°$), at $\vec{k}_{||} \sim 0.36$ ($\theta_e = 10°$) and $\sim 1.1$ Å$^{-1}$ ($\theta_e = 34°$) along the $\bar{\Gamma} - \bar{K}$ direction are shown in (b) and (c). (b) shows the results for the electrons with $\vec{P}$ parallel to the surface and perpendicular to the $\bar{\Gamma} - \bar{K}$ direction, and (c) for those with $\vec{P}$ perpendicular to the surface. (d) shows the SARIPE spectra at $\vec{k}_{||} \sim 1.07$ Å$^{-1}$ ($\theta_e = 60°$) for electrons with $\vec{P}$ perpendicular to the surface. (e) displays the hypothetical spin texture of one of the normal RB bands. (The arrows show the $\vec{P}$, as derived from the normal RB effect.)

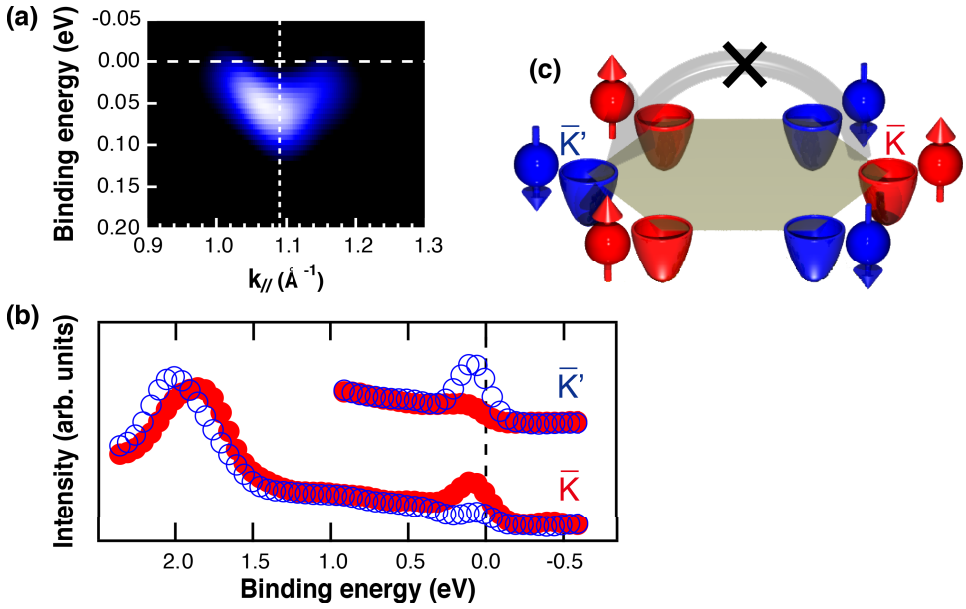


Figure 5: (a) ARPES data of the surface band at the $\bar{K}$ point of Tl/Si(111)-(1×1) with an additional Tl coverage of 0.12 ML. (b) SARPES spectra at $\bar{K}$ and $\bar{K}'$. (c) Schematic illustrations of the inter valley scattering.

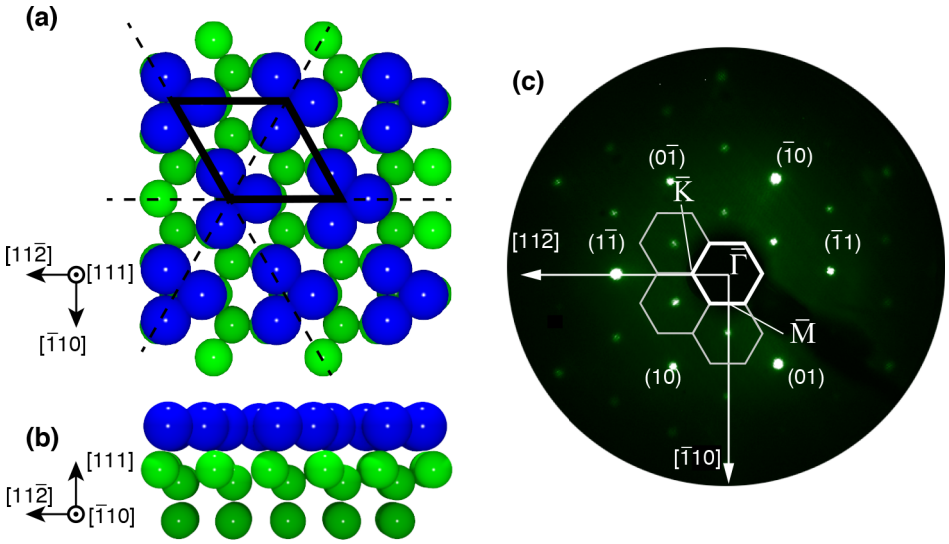


Figure 6: (a) Top view and (b) side view of $\beta$-Bi/Si(111)-($\sqrt{3} \times \sqrt{3}$). Blue and green circles indicate the Bi and Si atoms, respectively. The diamond shape and dashed lines represent the ($\sqrt{3} \times \sqrt{3}$) unit cell and the three mirror planes. (c) The LEED pattern, obtained with a primary electron energy of 80 eV, and the Brillouin zone of $\beta$-Bi/Si(111)-($\sqrt{3} \times \sqrt{3}$). The bold hexagon represents the first Brillouin zone and the thin ones are the second Brillouin zones.

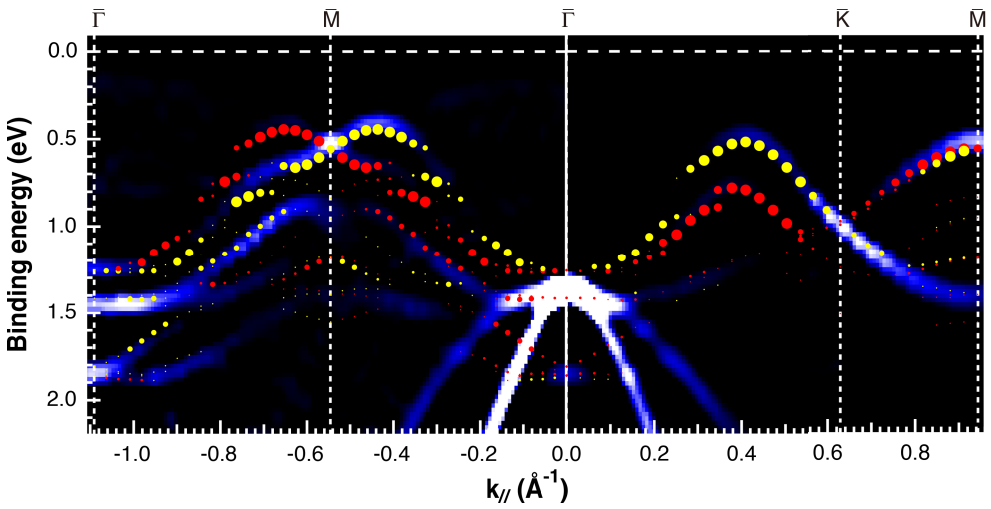


Figure 7: Band structure of $\beta$-Bi/Si(111)-($\sqrt{3} \times \sqrt{3}$) along $\bar{\Gamma} - \bar{M} - \bar{\Gamma} - \bar{K} - \bar{M}$. The red and yellow filled circles overlapping the experimentally obtained ARPES data are the spin-polarized electronic states obtained theoretically. The size of the red and yellow filled circles represents the polarization degree of spins that are parallel to the surface and perpendicular to the measuring direction, and the two colors correspond to the opposite two $\vec{P}$s. $\bar{\Gamma}$, $\bar{M}$, and $\bar{K}$ are the symmetry points of the ($\sqrt{3} \times \sqrt{3}$) Brillouin zone. The parabolic bands with downward dispersions around $\bar{\Gamma}$ are the Si bulk bands.

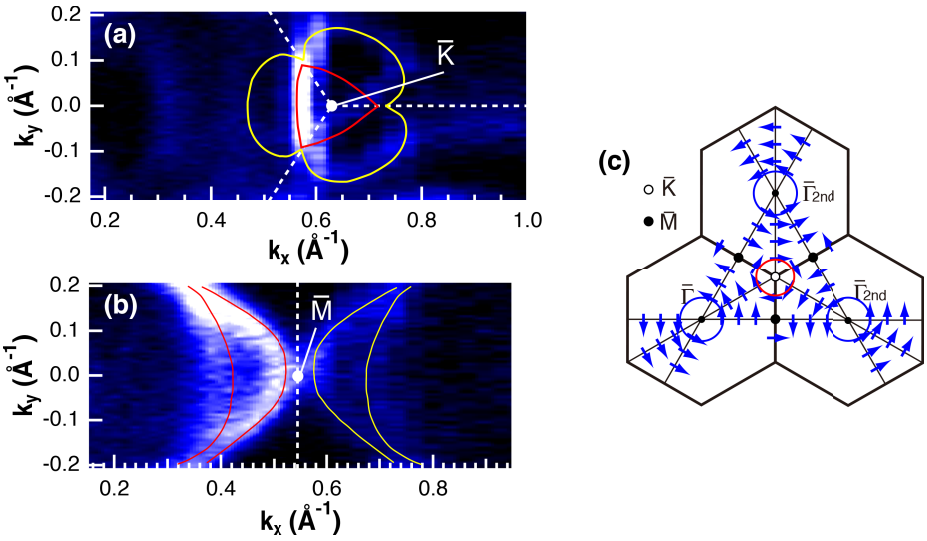


Figure 8: Constant energy contours (a) around $\bar{K}$ at $E_B = 0.85$ eV along the $\bar{\Gamma} - \bar{K} - \bar{M}$ direction, and (b) around $\bar{M}$ at $E_B = 0.45$ eV along $\bar{\Gamma}$-$\bar{M}$-$\bar{\Gamma}$. The dashed lines in (a) and (b) are the Brillouin zone boundaries. (c) A schematic illustration of the RB spin on Bi/Si(111)-$(\sqrt{3} \times \sqrt{3})$. The arrows show the $\vec{P}$ of one of the split bands, as derived from the normal RB effect.

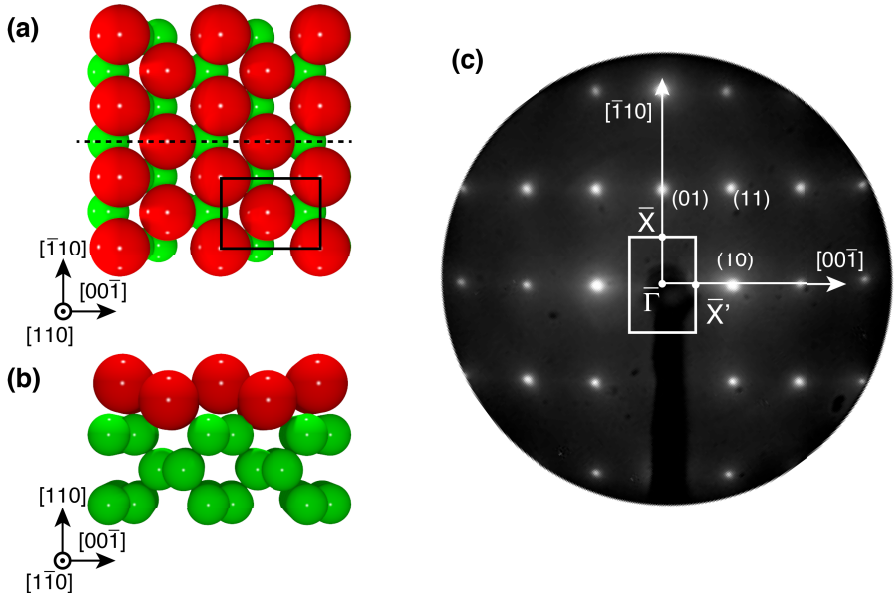


Figure 9: (a) Top- and (b) side-view of the atomic structure of Tl/Si(110)-(1×1). The large red and small green circles indicate Tl and Si atoms, respectively, and the rectangle in the top view (a) shows the (1×1) unit cell. The horizontal dashed line indicates the mirror plane. (c) LEED pattern of Tl/Si(110)-(1×1); the solid rectangle indicates the Brillouin zone, and $\bar{\Gamma}$, $\bar{X}$ and $\bar{X}'$ are the symmetry points of the Brillouin zone.

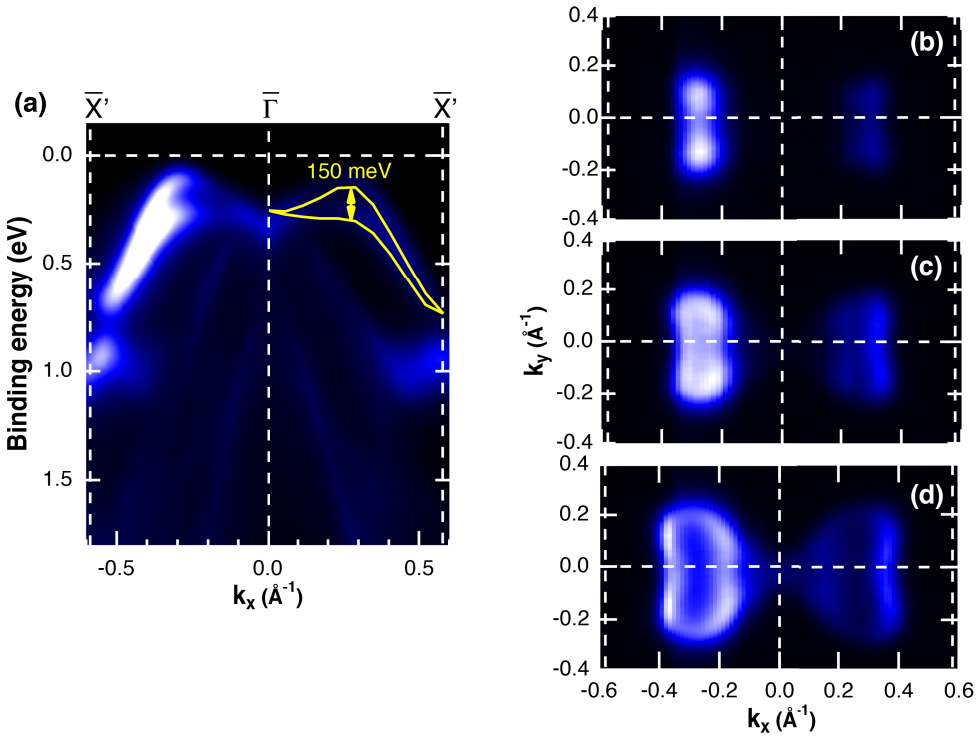


Figure 10: (a) Band structure of Tl/Si(110)-(1 × 1) measured along the $\bar{X}'$-$\bar{\Gamma}$-$\bar{X}'$ direction, and (b)-(d) characteristic energy contours, i.e., $k_x$-$k_y$ band mapping, at $E_B$ =50, 100 and 200 meV measured at $h\nu = 40$ eV. $k_x$ corresponds to the direction along $\bar{X}'$-$\bar{\Gamma}$-$\bar{X}'$ and $k_y$ to that along $\bar{X}$-$\bar{\Gamma}$-$\bar{X}$.

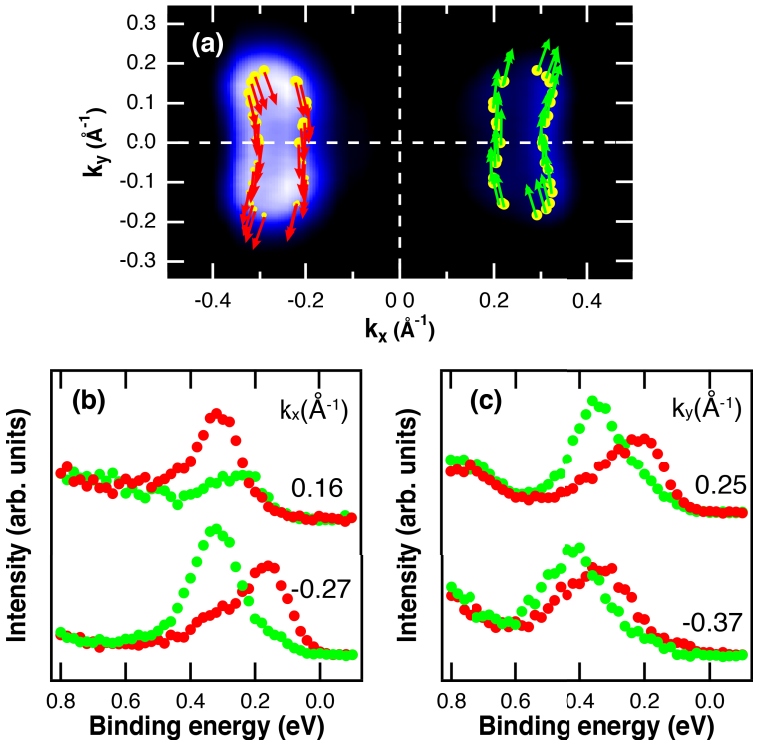


Figure 11: (a) Constant energy contour at $E_B = 0.1$ eV with superimposed the spin structure obtained theoretically. The arrows in (a) indicate the spin orientation. (b) SARPES spectra along $k_x$ at $k_y = 0$ and (c) along $k_y$ at $k_x = -0.27$ Å$^{-1}$. $k_x$ corresponds to the $[00\bar{1}]$ direction, i.e along $\bar{X}'$-$\bar{\Gamma}$-$\bar{X}'$, and $k_y$ to the $[\bar{1}10]$, i.e. along $\bar{X}$-$\bar{\Gamma}$-$\bar{X}$.

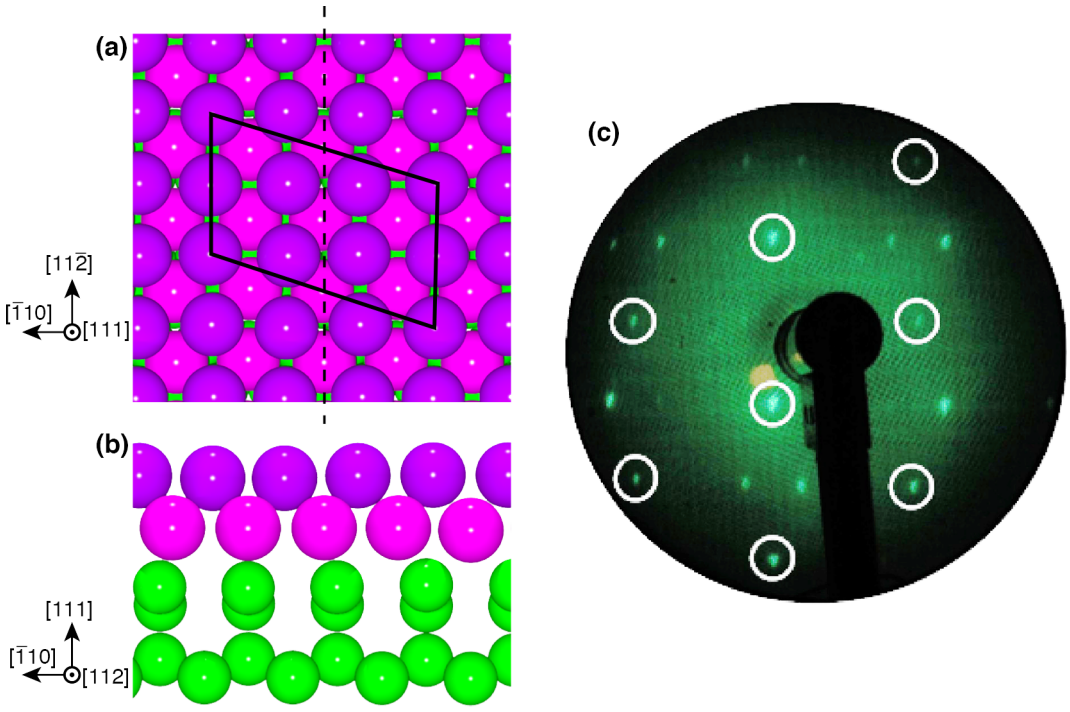


Figure 12: (a) Top- and (b) side-view of the atomic structures of In/Si(111)-($\sqrt{7} \times \sqrt{3}$). The solid line is the unit cell and the dashed line indicates the mirror plane. (c) LEED pattern of the sample used in the present study obtained with a primary energy of 85 eV at 300 K. The spots framed with circles are the fundamental spots of Si(111) and the extra ones are the result from the ($\sqrt{7} \times \sqrt{3}$) periodicity.

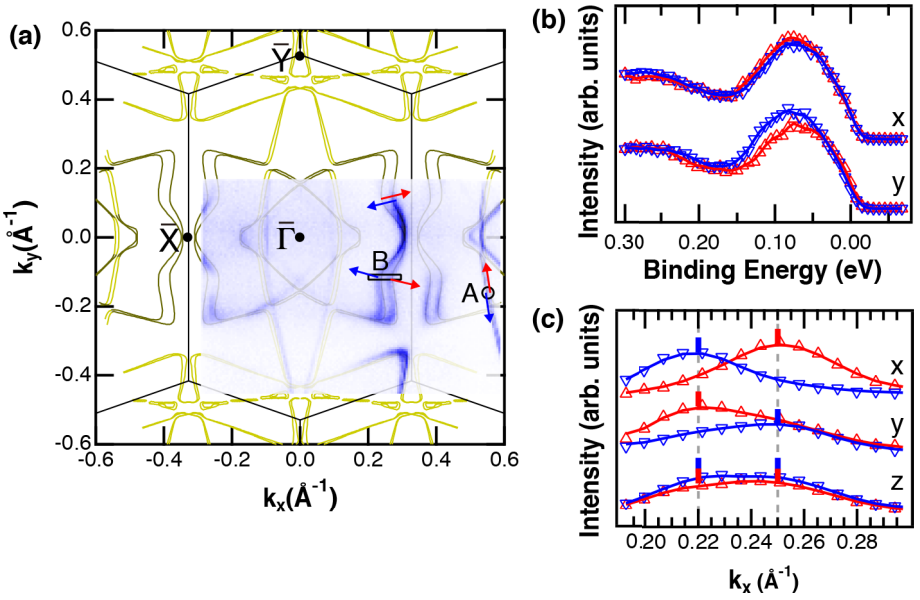


Figure 13: (a) The FS of In/Si(111)-($\sqrt{7} \times \sqrt{3}$). The theoretical calculation (khaki and dark khaki solid lines) is overlaid by the experimental data. Black solid lines are the Brillouin zone. $\bar{\Gamma} - \bar{Y}$ corresponds to the [11$\bar{2}$] direction, and $\bar{X} - \bar{\Gamma}$ to the [1$\bar{1}$0] direction. (b) Spin-resolved EDCs measured at the point A in the FS shown in (a), and (c) the spin-resolved MDCs measured at the cuts B. $x$, $y$, and $z$ axes correspond to the [1$\bar{1}$0], [11$\bar{2}$], and [111] directions of the substrate. Red (blue) data indicate spins in the positive (negative) direction of each axis. The red and blue bars and the gray dashed lines in (c) mark the peak positions in each spectrum and the corresponding $k_x$ values of the FS obtained by ARPES.

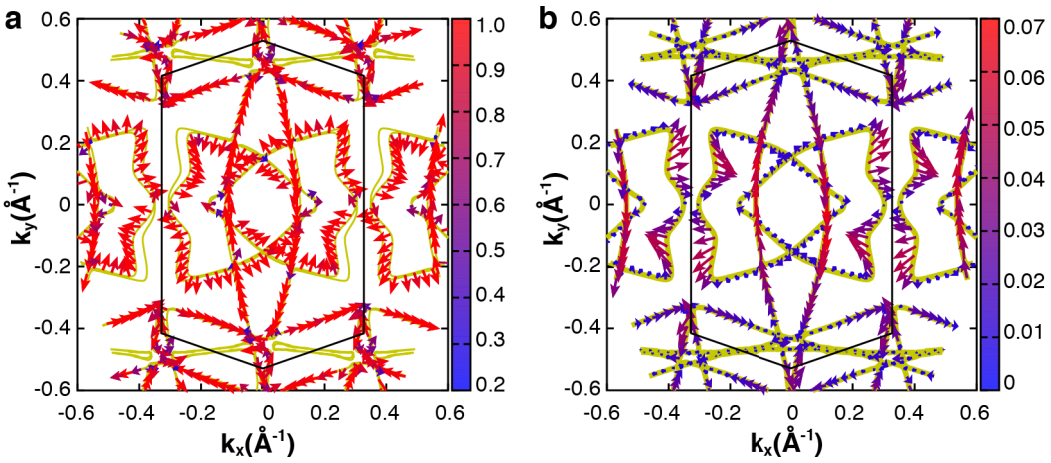


Figure 14: (a) Theoretically obtained spin polarization (arrows) of the FS (inner side only) in the presence of SOC and (b) theoretical OAM distribution (arrows) in the absence of SOC.

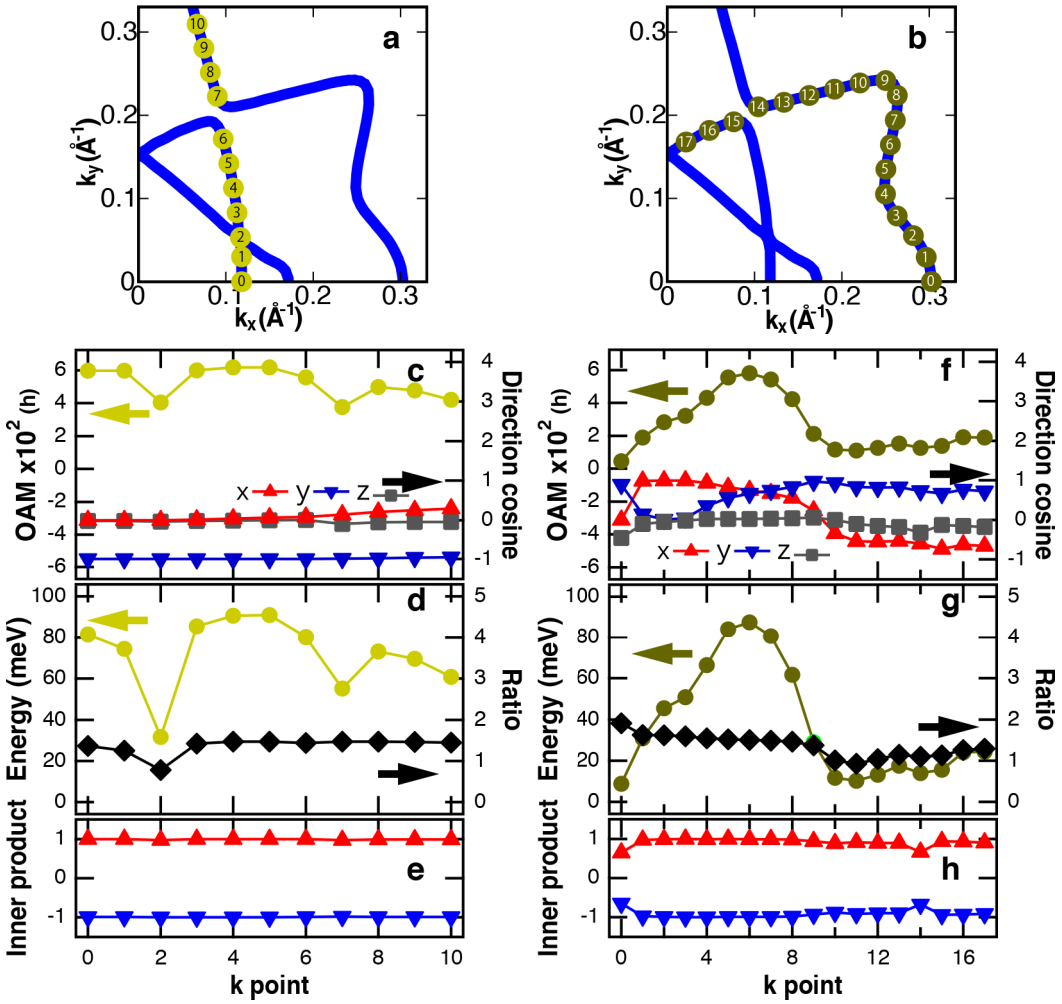


Figure 15: The size and direction of OAM ((c) and (f)), the spin splitting in energy and the ratio between this splitting and the size of OAM ((d) and (g)), and the inner product of the OAM and spin vector ((e) and (h)). The number given at the bottom axes of (c-h) corresponds to the $\vec{k}$ points labeled by the same number in (a) and (b).

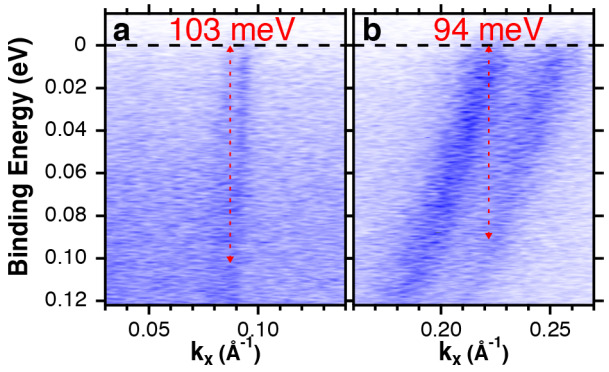


Figure 16: Band dispersions of (a) the $\vec{k}$ point 4 of the circular FS shown in Fig. 15(a), and (b) the $\vec{k}$ point 6 of the butterfly FS shown in Fig. 15(b).